Microscopic collective dynamics in liquid neon-deuterium mixtures: Inelastic neutron scattering and quantum simulations

Daniele Colognesi ●,[1,*] Ubaldo Bafile ●,[1] Eleonora Guarini ●,[2] Tatiana Guidi ●,[3] and Martin Neumann ●[4]

[1]*Consiglio Nazionale delle Ricerche, Istituto di Fisica Applicata "N. Carrara," I-50019 Sesto Fiorentino, Italy*
[2]*Dipartimento di Fisica e Astronomia, Università di Firenze, I-50019 Sesto Fiorentino, Italy*
[3]*ISIS Neutron and Muon Source, Rutherford Appleton Laboratory, Science and Technology Facilities Council,*
Harwell Oxford, Didcot OX11 0QX, United Kingdom
[4]*Fakultät für Physik der Universität Wien, A-1090 Wien, Austria*

In this paper a combined neutron scattering and quantum simulation study of the collective dynamics in liquid Ne-D_2 mixtures, at a temperature of $T = 30$ K and in the wave-vector transfer range 4 nm^{-1} < q < 51 nm^{-1}, is presented. Two D_2 concentrations are investigated, one close to 25% molar and the other close to 50% molar, together with pure Ne. The dynamic structure factor for the centers of mass of the two molecular species is extracted from the neutron scattering data and subsequently compared with that obtained from three different quantum simulation methods, such as *ring polymer molecular dynamics* and two slightly different versions of the Feynman-Kleinert approach. A general agreement is found, even though some discrepancies both among simulations, and between simulations and experimental data, can be observed. In order to clarify the physical meaning of the present spectroscopic results, an analysis of the longitudinal current spectral maxima is carried out showing the peculiarities of the D_2 center-of-mass dynamics in these mixtures. A comparison with the *centroid molecular dynamics* results obtained for the D_2 center-of-mass self-dynamics in the same liquid mixtures is finally proposed.

I. INTRODUCTION

The role of quantum effects in the behavior of solid and liquid solutions can be understood by studying alloys and mixtures of nuclear-spin species (e.g., *ortho*-H_2–*para*-H_2), isotopes (e.g., H_2-D_2), as well as quantum systems doped with appropriate substances [1]. However, due to the limited range of solubility for the different lightweight species, the choice is usually quite restricted. For example, as far as pressure changes are concerned, a relevant solubility that would be detectable in a variation of the microscopic properties of the mixture can, in general, be hardly expected. Nevertheless, mixtures of hydrogen, deuterium, and neon appear to represent an interesting exception [2,3]. As a matter of fact, since the molecular parameters (i.e., σ and ϵ) of the Lennard-Jones potential of hydrogen, deuterium, and neon are either identical (for H_2 and D_2) or very close (for H_2 and Ne) [4], theory can treat solutions of H_2, D_2, and Ne as isotopic or pseudoisotopic, respectively. For this reason, since the early 1990s there has been some interest in H_2-D_2 and H_2-Ne mixtures [5] but for the latter mainly in the solid phase and with a high hydrogen concentration. In the H_2-Ne system strong anomalies were detected in the temperature dependence of the heat capacity, and experimental data have been described assuming a variation of the Ne-H_2 force constant by a factor bigger than 2 with respect to that of pure H_2. Similar results have been found with D_2

replacing H_2, but in this case the correction factor amounts to 1.6 only. These values, although obtained through the pseudoharmonic approximation, have to be considered as very large since, as already mentioned, intermolecular potentials are indeed similar [4]. Thermodynamic evidence of a non-ideal character of such mixtures suggests that we investigate in greater detail the possible presence of purely dynamical effects, as those found, for example, in the phonon dispersion curves of solid H_2-D_2 systems [6]. There are some clues that this kind of effects should be common to H_2-D_2, H_2-Ne, and D_2-Ne solutions also in other thermodynamic conditions (e.g., in the liquid state). In addition, it is likely that the dynamic structure factor [7] (and, from it, the collective-excitation dispersion curves) are better probes than heat capacity alone, since they are more directly affected by the quantum particle delocalization, i.e., by the main microscopic property that distinguishes between a classical and a semiquantum fluid like H_2, D_2, and Ne. As for H_2-D_2 liquid mixtures, these intuitions were confirmed by incoherent inelastic neutron scattering experiments, where the spectrum of the velocity autocorrelation function of the H_2 centers of mass (i.e., an equivalent of the density of phonon states in solids) has been extracted and compared to the same quantity in pure liquid hydrogen, revealing peculiar and unexpected changes [8]. Similarly, although more extreme, findings have been recently detected in liquid H_2/Ne mixtures at low hydrogen concentrations (3–10% molar), where pseudocaging effects (caused by heavy neon atoms) impress on the H_2-velocity autocorrelation function an evident solidlike character [9]. Surely coherent neutron

_____
*Corresponding author: d.colognesi@ifac.cnr.it

scattering can provide a much richer and more detailed picture than the one so far obtained from single-particle spectroscopy, but, given the strong incoherent signal from H_2, the only amenable system turns out to be the D_2-Ne mixture, which is the subject of the present study. This paper also provides an extension to the case of mixtures of a very recent study [10] of the pure liquid D_2 collective dynamics, where inelastic neutron scattering was exploited together with the same quantum simulation techniques that have been applied here.

The rest of the present paper will be organized as follows: The experimental procedure will be described in detail in Sec. II, where the data reduction method will be also presented. Then Sec. III will be fully devoted to the computational details concerning the quantum dynamics simulations performed on the D_2-Ne mixtures under investigation in order to extract both the collective response of the system (i.e., the intermediate scattering functions [7]) and the self one (more precisely, the velocity autocorrelation functions which can be directly related to the self-intermediate scattering functions [7]). In Sec. IV, we will discuss the obtained results, and some key physical quantities derived from the experimental spectra will be contrasted with their estimates obtained from the mentioned quantum simulations. In addition, a comparison between the coherent spectra of the present study on D_2-Ne mixtures and the incoherent ones from H_2-Ne mixtures will be provided. Finally, Sec. V will be devoted to conclusions and perspectives.

II. EXPERIMENTAL DETAILS AND DATA REDUCTION

The present inelastic neutron scattering measurements [11] were performed on the MARI beamline [12], a spectrometer installed at the ISIS Neutron and Muon Source (Rutherford Appleton Laboratory, Science and Technology Facilities Council, United Kingdom). The MARI beamline is a direct-geometry spectrometer using the time-of-flight principle: The incoming neutron energy, E_i, is selected by a Fermi chopper before the scattering event, while the final neutron energy, E_f, is determined from the time of arrival of the scattered neutron in one of the detectors. This spectrometer has recently undergone a major instrument upgrade, which included new neutron guides, chopper system, and detector electronics, and has achieved flux gains ranging from 2 up to 20 depending on the incident energy with respect to the original version of MARI. In addition, the so-called *repetition rate multiplication* [13] is now a viable option, allowing for the possibility to use more than one value of E_i at the same time. In our case the pair $E_i = 7.1$ meV and 40.0 meV has been selected. The angular detection range available on MARI, expressed by the scattering angle θ, is $3° \leqslant \theta \leqslant 135°$ and is covered by an array of ^{3}He tubes with a step of about $0.4°$. With such an arrangement two different zones of the kinematic plane became accessible, namely those enclosed by the following rectangles: 5.75 nm$^{-1} \leqslant q \leqslant 50.75$ nm^{-1}, -10 meV $\leqslant \hbar\omega \leqslant 38.3$ meV and 4.0 nm$^{-1} \leqslant q \leqslant 25.0$ nm^{-1}, -3 meV $\leqslant \hbar\omega \leqslant 5.9$ meV, where $\hbar\omega$ stands for the energy transfer and q for the modulus of the wave-vector transfer. The MARI energy transfer resolution (i.e., the full width at half maximum $\Delta\hbar\omega$) is determined by various factors, including the

TABLE I. Experimental conditions of the measured samples, including sample number, title, temperature T, deuterium molar concentration $x[D_2]$, pressure p, total molecular density n, and integrated proton current (IPC). Estimated statistical uncertainties are listed in parentheses.

No.	Title	T (K)	$x[D_2]$ (%)	p (bar)	n (nm^{-3})	IPC (μA h)
(1)	Vanadium	299(1)	–	–	–	20.1
(2)	Empty cell	30.01(3)	–	–	–	2281.7
(3)	Liquid neon	30.02(3)	0.00	2.24(1)	34.43(1)	1699.0
(4)	Liquid D_2/Ne	30.01(3)	23(1)	4.97(3)	28.9(3)	1873.8
(5)	Liquid D_2/Ne	30.03(3)	49(4)	6.3(8)	24.8(5)	2363.6

incoming neutron energy, the chopper spinning frequency, and the type of Fermi chopper used for the measurement. In our case a G-chopper (made of alternating neutron-transmitting slits and neutron-absorbing gadolinium slits) spinning at a frequency of 400 Hz was employed, giving rise to $\Delta\hbar\omega$ values at $\omega = 0$ (i.e., the so-called *elastic line* resolution) ranging from 1.70 meV at the lowest scattering angle up to 2.80 meV at the highest one, and from 0.19 meV up to 0.33 meV, for $E_i = 40.0$ meV and 7.1 meV, respectively. They have been experimentally determined via appropriate vanadium measurements. As for the $\Delta\hbar\omega$ values at $\omega \neq 0$, one has to rely on numerical estimates obtained from routines available on the spectrometer.

A detailed description of the measured samples (including temperature T, deuterium molar concentration $x[D_2]$, pressure p, and total molecular density n) is reported in Table I, where the last quantity has been estimated using various thermodynamic data sets available in the literature: Reference [14] for pure Ne, Ref. [15] for pure deuterium, and, finally, Ref. [16] and Ref. [17] for the nonideal behavior of the D_2-Ne mixtures. In addition, the thermodynamic data presented in the last two references have been checked and extrapolated making use of the path-integral Monte Carlo technique (PIMC) [18] performed in an isothermal-isobaric ensemble in order to estimate the mixture density and its changes along with the D_2 concentration. As for the relative concentration of *ortho-* and *para-*deuterium species, which determines the population of the molecular rotational states, we have always assumed that deuterium is in the "normal" (*n-*D_2) state in the present experiment. In *n-*D_2 the *ortho-para* population is not in thermodynamic equilibrium at $T = 30$ K but still the one at room temperature: $x[o\text{-}D_2]/x[p\text{-}D_2] = 2$. This is possible since liquid normal deuterium is metastable at low temperature because the spontaneous *para*-to-*ortho* conversion proceeds extremely slowly with a typical time of the order of several weeks (see Fig. 9-1 in Ref. [19]), when appropriate paramagnetic catalysts are not present. Nevertheless, the deuterium stability during the experiment has been checked by comparing consecutive subruns of the individual neutron scattering measurements for the mixture samples [i.e., Nos. (4) and (5) in Table I].

After a standard calibration measurement of an appropriate vanadium annulus, we recorded a statistically accurate empty-cell spectrum at low temperature. The scattering cell was a

cylindrical container made of aluminum (namely, AA7075) exhibiting an annular cross section with a 2.0-mm void to be filled with the liquid sample, which in this way occupied an interspace with an average diameter of 41.0 mm. The internal cell volume was estimated to be 12.85 cm^3, while each metallic wall was 1.0 mm thick. As the container was placed horizontally, its external diameter roughly coincided with the vertical beam size (about 45 mm), while its length (70.0 mm) was rather larger than the horizontal beam size (also about 45 mm), so the cell was masked with boron nitride ceramics excluding both ends which actually contained no sample. Pure liquid neon was the first sample to be measured. It was prepared by condensing Ne gas (4.5 grade, equivalent to a 99.995% assay) into the cell kept at $T = 33.0$ K. Then its temperature was slowly decreased to the value of $T = 10.0$ K where the pressure of the gas handling system reached the final value of $p = 0.18$ bar, with frozen neon filling up completely the sample container. Finally, the temperature was raised to $T = 30.0$ K, the pressure was adjusted to $p = 2.24$ bar, and the measurement of sample No. (3) began (see Table I for other details). Concerning the two mixed samples, namely Nos. (4) and (5) as in Table I, the measurement procedure was slightly more complex. We will focus on sample No. (4) ($x[D_2] = 23\%$), noting that sample No. (5) ($x[D_2] = 49\%$) was prepared and measured in quite a similar way. Appropriate amounts of deuterium gas (99.995% assay, 99.8% isotopic purity) and neon gas were mixed in four buffer volumes (1 liter each) at room temperature under a pressure of $p = 3.43$ bar. These values corresponded to the exact amount of gaseous mixture needed to fill up our cell with liquid at a working temperature of $T = 30.0$ K. The cell was initially kept at $T = 36.0$ K and connected to the buffer volumes through the gas handling system, then it was slowly cooled down to $T = 4.0$ K, monitoring the vapor pressure and waiting (after some hours) until it reached its final equilibrium value of few millibars. At this stage, we were sure that the frozen mixture filled up completely the sample container with the correct D_2 concentration, since only a negligible amount of gaseous mixture had been left in the buffer volumes and the gas handling system. Finally, the sample container was isolated from the buffer volumes and warmed up to $T = 30.0$ K, where the internal pressure reached a stable value of 4.97 bar allowing for the start of the neutron measurement. Vapor pressure and sample temperature were monitored all the time, but in order to further check the sample stability (i.e., liquid density, D_2 concentration, and *ortho-para* composition, etc.) the run was divided in a series of subruns which were carefully compared to one another before being merged into a single data set.

Raw time-of-flight data produced by the MARI measurements of all samples were divided by the integrated proton current values, purged of noisy tube contributions, normalized to vanadium counts, and corrected for detector efficiency. Then these data sets were transformed into $\hbar\omega$ spectra and divided by the kinematic factor $\sqrt{E_f/E_i}$ [7]. At this stage, the spectra related to the three samples, namely Nos. (3)–(5) as in Table I, needed to undergo the following treatments:

  (i)   empty container scattering removal,
  (ii) sample self-shielding correction,
  (iii) multiple scattering removal.

Points (i) and (ii) were carried out using numerical routines which approximately calculated the attenuations of both the transmitted and the scattered beam caused by the sample cell in its two working conditions: empty and filled. An example of this procedure can be found in Fig. 1 for neutron data from sample No. (4) measured with $E_i = 40.0$ meV. The selected wave-vector transfer values, namely $q = 18.25$ and 35.75 nm^{-1}, have been chosen since, exhibiting intermediate scattering intensities, they can be considered as two representative cases. For the two D_2/Ne mixture samples [i.e., Nos. (4) and (5)] the total neutron scattering cross section was approximated by a simple linear combination of the cross section of neon [20], $\sigma_t[Ne]$, and that of liquid normal deuterium at $T = 19$ K [21], $\sigma_t[n\text{-}D_2](E_i)$, as no more accurate data were found in the literature. In this way, we have evaluated the following estimates of the neutron transmission with $E_i = 40.0$ meV (and $E_i = 7.1$ meV): 94.7% (94.6%), 93.7% (92.0%), and 92.8% (89.9%) for the three liquids forming samples Nos. (3), (4), and (5), respectively. As for point (iii), double scattering contributions were accurately simulated and subtracted through the analytical approach suggested by Agrawal and Sears [22], where its input, i.e., the macroscopic scattering law of the system, was estimated in the framework of the Sköld approximation [23], in conjunction with the modified Young-Koppel model for $n\text{-}D_2$ [24,25] and the Gaussian approximation [7] for the self-dynamics of Ne and the D_2 center of mass. The various physical quantities needed for such an approach have been obtained from the quantum simulations presented below in Sec. III. Experimental data have been finally arranged in constant-q spectra (also known as q slices) exhibiting the following slice thickness: $\Delta q = 2.5$ nm^{-1} for $E_i = 40.0$ meV and $\Delta q = 1.0$ nm^{-1} for $E_i = 7.1$ meV. Fully processed experimental spectra, $I_E(q, \omega)$, have been plotted in Figs. 2–4 for samples Nos. (3), (4), and (5), respectively.

III. QUANTUM DYNAMICS SIMULATIONS

In order to provide molecular dynamics spectra required for the study of the fully processed experimental data from samples Nos. (3)–(5), we performed four types of approximate quantum dynamics simulations, namely *centroid molecular dynamics* (CMD) [26], *ring polymer molecular dynamics* (RPMD) [27], *Feynman-Kleinert linearized path integral* (FK-LPI) [28], and *Feynman-Kleinert quasi-classical Wigner* (FK-QCW) dynamics [29], although the first method was employed only for ancillary applications related to the Ne and D_2 self-dynamics. All four methods are based on essentially exact (or very good approximations to the) quantum mechanical static distributions, but the dynamics is invariably classical. In CMD and RPMD the "classical isomorphism" of PIMC, which replaces each quantum particle by a classical, harmonically bound ring polymer of P (the Trotter number) copies of itself, is taken literally, i.e., the polymer centers (in the case of CMD) are allowed to evolve classically in the force field averaged over all possible monomer positions, whereas in RPMD it is the individual monomers whose equations of motion are integrated. Also, in CMD observables and correlation functions are evaluated at the polymer centers, whereas in RPMD averages over the observables' values at
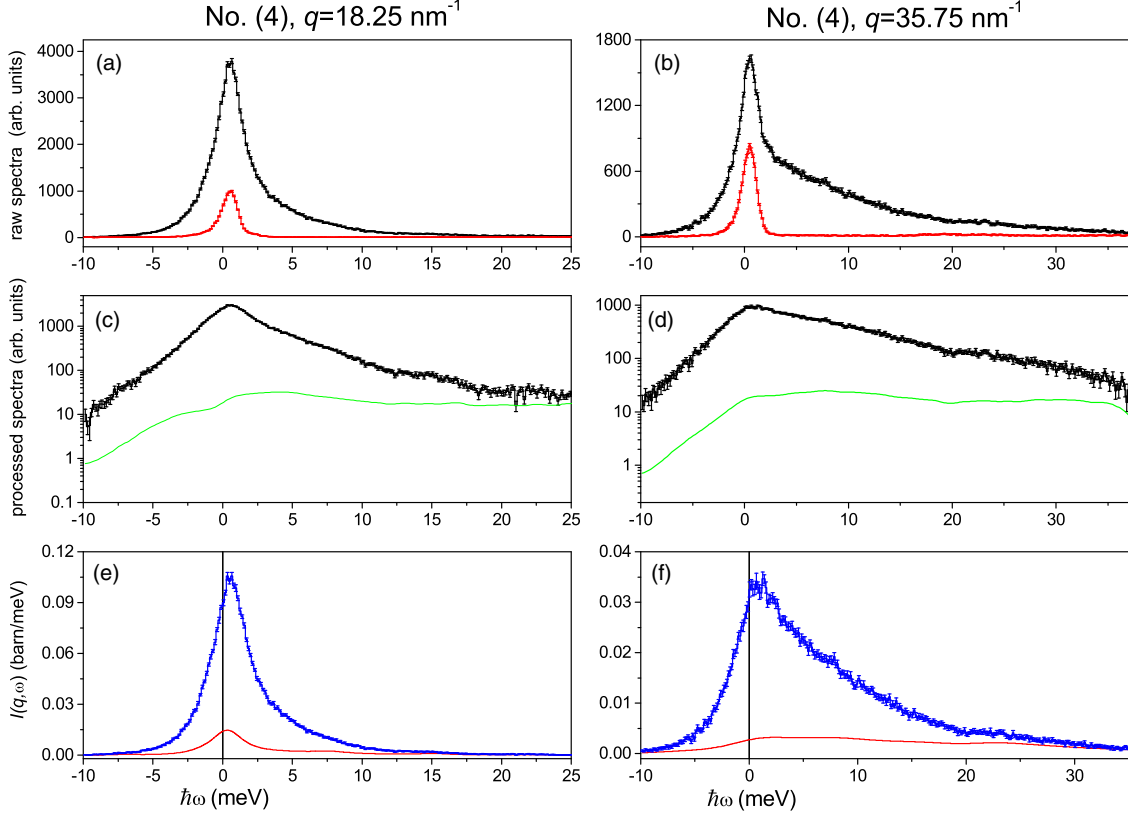
FIG. 1. Examples of the data reduction procedure explained in the main text and here applied to sample No. (4), measured with $E_i = 40.0$ meV: panels (a) and (b) describe the removal of the empty cell signal (red line and error bars) from the sample-plus-cell raw spectrum (black line and error bars); panels (c) and (d) show the subtraction of the simulated multiple scattering signal (green line) from the processed spectrum (black line and error bars); and panels (e) and (f) compare the simulated incoherent spectrum $I_{\mathrm{inc}}(q, \omega)$ from D_2 (red line) with the experimental one, $I_E(q, \omega)$ (blue line and error bars), containing both coherent and incoherent components. Panels (a), (c), and (e) and (b), (d), and (f) refer to q values equal to 18.25 and 35.75 nm^{-1}, respectively.

the monomer positions are taken. By contrast, in FK-LPI and FK-QCW time correlation functions are calculated along classical N-body "side" trajectories whose initial conditions are sampled from the Wigner transform of the Boltzmann operator. In FK-LPI the corresponding "center" trajectory is obtained from a Monte Carlo random walk, while in FK-QCW it is the result of a (classical) molecular dynamics simulation in phase space using the local Feynman-Kleinert effective potential [30] as a guiding function. Moreover, in FK-LPI the side trajectories are propagated independently under the influence of the classical Hamiltonian, whereas in FK-QCW they are coupled to, and "orbit" around, the center trajectory.

The first two techniques (i.e., CMD and RPMD) are computational tools able to provide good approximations of the Kubo-transformed correlation functions in many-body systems exhibiting weak or moderate quantum effects at $T > 0$, but both suffer the limitation that these correlation functions may include only operators which are linear either in the coordinates or in the momenta of the particles composing the system. It is worth recalling that the Kubo transform [31], $\lambda_{AB}^{(K)}(t)$, of a time correlation function $\lambda_{AB}(t)$, involving quantum operators $\hat{A}$ and $\hat{B}$, is given by:

$$\lambda_{AB}^{(K)}(t) = \frac{1}{\beta} \int_0^\beta dz \lambda_{AB}(t + i\hbar z), \qquad (1)$$

where $\beta = 1/(k_B T)$ and k_B is the Boltzmann constant. As a consequence, CMD and RPMD are not recommended for the estimate of either the intermediate scattering function $F(q, t)$ or the self-intermediate scattering function $F_s(q, t)$ [7], which are generally involved in the simulation of neutron scattering spectra, unless the value of the wave vector q is so low that the dependence on the particle coordinates can be approximately linearized. On the other hand, CMD and RPMD are suitable for the computation of the Kubo-transformed velocity autocorrelation function, $c^{(K)}(t)$, which can be used to evaluate $F_s(q, t)$ via the well-assessed Gaussian approximation [32]. A different approach to quantum time correlation functions is represented by the so-called *classical Wigner* models [33], in which the calculation is divided into two separate tasks, namely the generation of initial conditions and the propagation of the dynamics, where the former is done through the Wigner phase-space distribution, while the latter is approximated as classical. A conceptually as well as computationally convenient implementation of the classical Wigner models is the FK-LPI approach, which provides the real part of the quantum time correlation functions, rather than the Kubo transformed ones, and is not prone to the operator limitations affecting both RPMD and CMD. In addition, it rigorously complies with the scattering particle recoil [7], appearing in this way particularly suitable for lightweight masses like
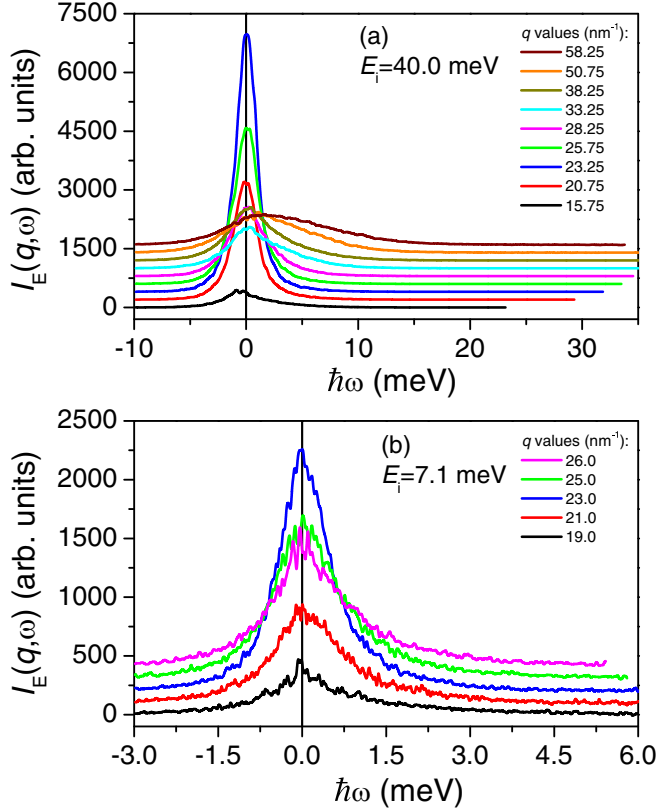
FIG. 2. Experimental neutron spectra (fully processed) for sample No. (3) (pure Ne, $T = 30.02$ K as in Table I) plotted for selected q values. Curves have been vertically shifted for graphic reasons. Panel (a) contains data measured with an incoming neutron energy $E_i = 40.0$ meV, from $q = 15.75$ nm^{-1} (bottom) to 58.25 nm^{-1} (top), while panel (b) shows those obtained with $E_i = 7.1$ meV, from $q = 19.0$ nm^{-1} (bottom) to 26.0 nm^{-1} (top).

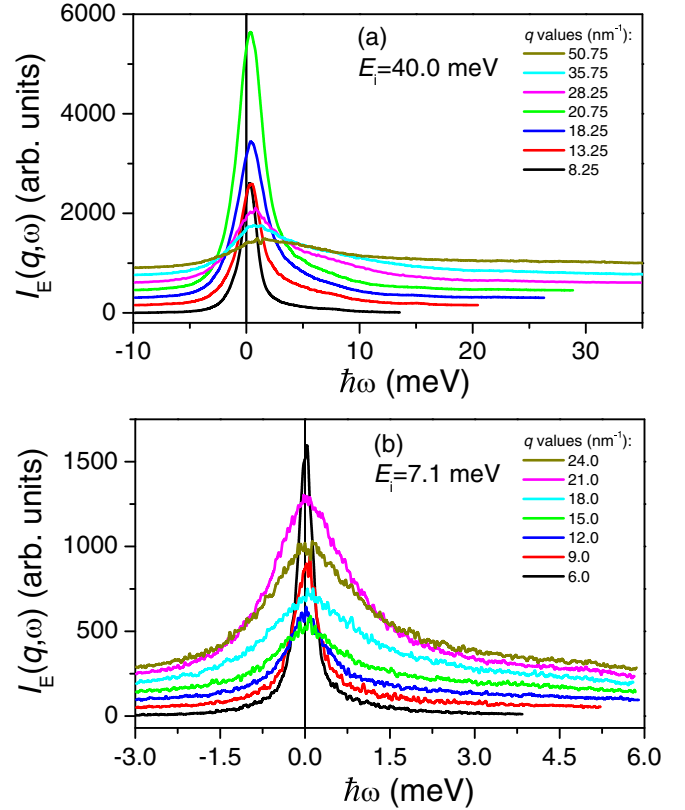FIG. 3. Experimental neutron spectra (fully processed) for sample No. (4) (D$_2$/Ne mixture, $x[\text{D}_2] = 23\%$, $T = 30.01$ K as in Table I) plotted for selected q values. Curves have been vertically shifted for graphic reasons. Panel (a) contains data measured with an incoming neutron energy $E_i = 40.0$ meV, from $q = 8.25$ nm^{-1} (bottom) to 50.75 nm^{-1} (top), while panel (b) shows those obtained with $E_i = 7.1$ meV, from $q = 6.0$ nm^{-1} (bottom) to 24.0 nm^{-1} (top).

hydrogen, deuterium, and helium. Finally, as far as the fourth quantum dynamics technique (i.e., FK-QCW) is concerned, this is a new approach also related to the classical Wigner approximation [33] and, although being computationally rather more demanding, it too does not suffer the mentioned linear operator limitation of RPMD and CMD. For this reason, both FK-LPI and FK-QCW have been already used to calculate the collective properties encapsulated in the $F(q, t)$ of semiquantum liquids such as neon [34], as well as pure hydrogen and deuterium [35].

Given this scenario, we used CMD to compute the $c_\alpha^{(K)}(t)$ for our samples [and from this, via the Gaussian approximation, $F_{s,\alpha}(q, t)$], RPMD mainly for the low-q limit of $F_{\alpha,\beta}(q, t)$ (i.e., q up to 27–30 nm^{-1}), and, finally, FK-LPI and FK-QCW (specifically, version FK-QCW(2) of Smith *et al.* [29]) for the full q range of the same physical quantities, where α and β can represent either a Ne atom or a D$_2$ center of mass (see Appendix for further details). In addition, standard PIMC simulations have been carried out in order to check the consistency of the quantum dynamic simulations by monitoring the partial static structure factors, $S_{\alpha,\beta}(q)$, and the single-particle mean kinetic energies, $\langle E_K \rangle_\alpha$. All the mentioned calculations have been performed at $T = 30.0$ K and at densities between 21.41 nm$^{-3} < n < 34.44$ nm^{-3}, depending

on the selected $x[\text{D}_2]$ value (see Table II for details). CMD has been performed in the isokinetic ensemble, RPMD in a canonical ensemble with Langevin thermostats, and in the Feynman-Kleinert methods initial conditions for the trajectories were sampled from distributions corresponding to the nominal temperature T, but the (classical) trajectories themselves were not thermostatted but allowed to evolve freely. As for the total number of molecules $N = N[\text{D}_2] + N[\text{Ne}]$, we chose $N = 256$ for CMD and RPMD, while for FK-LPI and FK-QCW, which are more computationally demanding, simulations were restricted to smaller particle numbers ($N = 108$). Consequently, the accessible wave vectors (i.e., those compatible with the cubic simulation volume) were different in the cases $N = 108$ and $N = 256$. Interparticle interactions have been taken to be pairwise additive according to the following scheme:

(a) Those between two Ne atoms were represented by a spherically symmetric Lennard-Jones potential using the Morales and Nuevo parametrization [36], which proved to be particularly effective for the H$_2$-Ne liquid mixtures [9,18].

(b) Those between a D$_2$ center of mass and a Ne atom were modeled by the spherical average of the orientation-dependent semiempirical potential developed by Faubel *et al.* [37], as suggested by Challa and Johnson [18] in the case of H$_2$-Ne liquid mixtures.
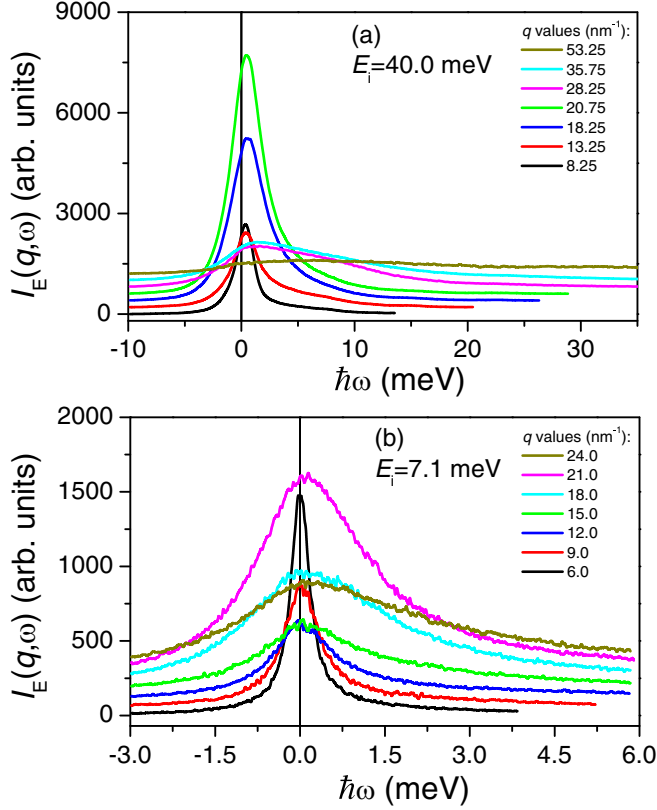
FIG. 4. Experimental neutron spectra (fully processed) for sample No. (5) (D_2/Ne mixture, $x[D_2] = 49\%$, $T = 30.03$ K as in Table I) plotted for selected q values. Curves have been vertically shifted for graphic reasons. Panel (a) contains data measured with an incoming neutron energy $E_i = 40.0$ meV, from $q = 8.25$ nm^{-1} (bottom) to 53.25 nm^{-1} (top), while panel (b) shows those obtained with $E_i = 7.1$ meV, from $q = 6.0$ nm^{-1} (bottom) to 24.0 nm^{-1} (top).

(c) Those between two D_2 centers of mass were described by the well-established spherically symmetric Silvera-Goldman potential [38].

While our velocity correlation functions were obtained from 10 CMD runs of 500 ps each at every thermodynamic state, all RPMD, FK-LPI, and FK-LPI results represent averages over 10 000 trajectories of 10 ps. In order to be consistent, an identical Trotter number of $P = 32$ was used for PIMC, CMD, and RPMD, and the number of "side trajectories" in FK-LPI and FK-QCW was also (arbitrarily) set to that number. Further computational details of our implementation of CMD and RPMD, as applied to semiquantum systems similar to the present ones, have been recently provided in Refs. [9] and [39], respectively, while concerning the two Feynman-Kleinert approaches, we have essentially followed the procedures reported in Ref. [34] for liquid neon and in Ref. [35] for liquid hydrogen and deuterium. In addition, a more complete description of these two techniques as well as the numerical routes used to implement them can be found in a recent paper on the liquid deuterium dynamics [10]. What is important to stress is the difference between the output of RPMD on one side and that of FK-LPI and FK-QCW on the other. In the case of a binary mixture the first technique produces three physical quantities, $F_{\alpha,\beta}^{(K)}(q,t)$, which approximate the Kubo transforms of the partial intermediate scattering functions, $F_{\alpha,\beta}(q,t)$. So the standard approach to work out the partial dynamic structure factors, $S_{\alpha,\beta}(q,\omega)$, was the following [31]:

$$S_{\alpha,\beta}(q,\omega) = \frac{\hbar\omega}{2k_BT}\left[\coth\left(\frac{\hbar\omega}{2k_BT}\right) + 1\right]\int_{-\infty}^{\infty}\frac{dt}{2\pi}$$
$$\times \exp(-i\omega t)F_{\alpha,\beta}^{(K)}(q,t). \qquad (2)$$

On the other hand, the last two techniques provide the (approximate) real parts of the intermediate scattering functions,

TABLE II. Thermodynamic conditions of the liquid samples simulated at $T = 30.00$ K and other details, including simulation number, total number of particles N, number of D_2 molecules $N[D_2]$, deuterium molar concentration $x[D_2]$, total molecular density n, type of technique used, and mean kinetic energy $\langle E_K\rangle$ from PIMC for D_2 center of mass and Ne.

No.	N	$N[D_2]$	$x[D_2]$ (%)	n (nm^{-3})	PIMC	CMD	RPMD	FK-LPI	FK-QCW	$\langle E_K\rangle_{D_2}$ (K)	$\langle E_K\rangle_{Ne}$ (K)
(i)	108	0	0.00	34.44	Y	–	–	Y	Y	–	54.14
(ii)	108	16	14.81	30.71	Y	–	–	–	Y	72.57	52.64
(iii)	108	27	25.00	28.60	Y	–	–	Y	Y	69.45	51.85
(iv)	108	38	35.19	26.80	Y	–	–	–	Y	67.14	51.22
(v)	108	49	45.37	25.28	Y	–	–	Y	Y	65.35	50.65
(vi)	108	54	50.00	24.67	Y	–	–	Y	Y	64.63	50.43
(vii)	108	59	54.63	24.12	Y	–	–	Y	Y	64.04	50.18
(viii)	108	81	75.00	22.33	Y	–	–	–	Y	62.04	49.49
(ix)	108	108	100.00	21.41	Y	–	–	Y	Y	60.81	–
(I)	256	0	0.00	34.44	Y	Y	Y	–	–	–	54.27
(II)	256	38	14.84	30.71	Y	Y	Y	–	–	72.40	52.70
(III)	256	64	25.00	28.60	Y	Y	Y	–	–	69.52	52.04
(IV)	256	90	35.16	26.80	Y	Y	Y	–	–	67.09	51.29
(V)	256	115	44.92	25.34	Y	Y	Y	–	–	65.48	50.81
(VI)	256	141	55.08	24.07	Y	Y	Y	–	–	63.98	50.24
(VII)	256	192	75.00	22.33	Y	Y	Y	–	–	62.10	49.54
(VIII)	256	256	100.00	21.41	Y	Y	Y	–	–	60.90	–

$\mathrm{Re}[F_{\alpha,\beta}(q,t)]$, and the relationship to obtain the dynamic structure factors [40] becomes

$$S_{\alpha,\beta}(q,\omega) = \exp\left(\frac{\hbar\omega}{2k_BT}\right)\mathrm{sech}\left(\frac{\hbar\omega}{2k_BT}\right)\int_{-\infty}^{\infty}\frac{dt}{2\pi}\exp(-i\omega t)\mathrm{Re}[F_{\alpha,\beta}(q,t)]. \tag{3}$$

As for the self-dynamic structure factors $S_{s,\alpha}(q,\omega)$, the expression provided by the Gaussian approximation [32] is

$$S_{s,\alpha}(q,\omega) = x[\alpha]\int_{-\infty}^{\infty}\frac{dt}{2\pi}\exp(-i\omega t)\exp\left(-\frac{\hbar q^2}{2M_\alpha}\int_0^{\infty}\frac{f_\alpha(\epsilon)}{\epsilon}\left\{\coth\left(\frac{\hbar\epsilon}{2k_BT}\right)[1-\cos(\epsilon t)]-i\sin(\epsilon t)\right\}d\epsilon\right), \tag{4}$$

where $x[\alpha]$ is the concentration of the α species, M_α is its molecular mass, and $f_\alpha(\epsilon)$ is a spectral function directly related to the velocity correlation function $c_\alpha^{(K)}$:

$$f_\alpha(\omega) = \frac{2}{c_\alpha^{(K)}(0)}\int_{-\infty}^{\infty}\frac{dt}{2\pi}\exp(-i\omega t)c_\alpha^{(K)}(t). \tag{5}$$

Once $S_{\alpha,\beta}(q,\omega)$ and $S_{s,\alpha}(q,\omega)$ have been obtained, the simulated neutron scattering spectra $I(q,\omega)$ can be worked out after splitting them into their coherent and incoherent components: $I(q,\omega) = I_{\mathrm{coh}}(q,\omega) + I_{\mathrm{inc}}(q,\omega)$ and taking into account the diatomic structure of the D_2 molecule. In our context the coherent component is given by:

$$I_{\mathrm{coh}}(q,\omega) = \left[(b_c[\mathrm{Ne}])^2 S_{\mathrm{Ne,Ne}}(q,\omega)\right.$$
$$+ 2b_c[\mathrm{Ne}]\sqrt{u(q)}S_{\mathrm{Ne,D_2}}(q,\omega)$$
$$\left.+ u(q)S_{D_2,D_2}(q,\omega)\right] \otimes R_q(\omega), \tag{6}$$

where $b_c[\mathrm{Ne}]$ is the coherent scattering length for natural neon [20], $u(q)$ is the so-called *intermolecular cross section* for deuterium [24,25], and $R_q(\omega)$ represents the instrumental energy transfer resolution which is convoluted with the simulation spectra. A good approximation for $u(q)$ is simply given by $u(q) \approx [2b_c[\mathrm{D}]j_0(qd_0/2)\exp(-q^2\langle u^2\rangle_v/3)]^2$, where $b_c[\mathrm{D}]$ is the coherent scattering length for D, $j_0(x)$ is a spherical Bessel function of zeroth order, d_0 is the D_2 interatomic distance, and $\langle u^2\rangle_v$ is the atomic vibrational mean-square displacement in D_2, defined, e.g., in Ref. [25]. The incoherent component, considering the tiny value of the Ne incoherent scattering cross section [20], can be safely approximated by the deuterium contribution alone, which, together with the self-dynamics of the D_2 centers of mass, also contains the details of the n-D_2 rotational dynamics. Making use of the mentioned modified Young-Koppel model [24,25], one can decouple these two dynamic terms and write:

$$I_{\mathrm{inc}}(q,\omega) = \left\{[\tilde{v}(q,\omega) - u(q)\delta(\omega)] \otimes S_{s,D_2}(q,\omega)\right\} \otimes R_q(\omega), \tag{7}$$

where $\tilde{v}(q,\omega)$, which is the Fourier transform of the time-dependent *intramolecular cross section* [24,25] for n-D_2, $v(q,t)$, can be represented as:

$$\tilde{v}(q,\omega) = \sum_{J,J'} x_J f_{J,J'}(q)\delta(\omega - \omega_{J,J'}), \tag{8}$$

with J and J' being the initial and final rotational quantum number, respectively, and where x_J is the concentration of the rotational population labeled by the quantum number J, $f_{J,J'}(q)$ is the matrix element for the $J \to J'$ transition, and $\hbar\omega_{J,J'}$ is the energy jump for such a transition. The energy-transfer integral of $I_{\mathrm{inc}}(q,\omega)$ can be evaluated analytically [24,25], and a good approximation for normal deuterium is given by:

$$I_{\mathrm{inc}}(q) = \int_{-\infty}^{\infty}I_{\mathrm{inc}}(q,\omega)d\omega = v(q,0) - u(q)$$
$$= \left[2(b_i[\mathrm{D}])^2 + 2(b_c[\mathrm{D}])^2 + 2(b_c[\mathrm{D}])^2 j_0(qd_0)\right.$$
$$\left.\times \exp\left(-\frac{4}{3}q^2\langle u^2\rangle_v\right)\right] - u(q), \tag{9}$$

where $b_i[\mathrm{D}]$ is the incoherent scattering length for D [20]. As for the energy-transfer integral of $I_{\mathrm{coh}}(q,\omega)$, dubbed $I_{\mathrm{coh}}(q)$, from Eq. (6) one readily obtains:

$$I_{\mathrm{coh}}(q) = (b_c[\mathrm{Ne}])^2 S_{\mathrm{Ne,Ne}}(q) + 2b_c[\mathrm{Ne}]\sqrt{u(q)}S_{\mathrm{Ne,D_2}}(q)$$
$$+ u(q)S_{D_2,D_2}(q), \tag{10}$$

which contains only static structural data. Using the mentioned PIMC estimates of $S_{\alpha,\beta}(q)$, we can now calculate the neutron-simulated structure factor $I(q)$, given by the sum of $I_{\mathrm{coh}}(q)$ and $I_{\mathrm{inc}}(q)$, for the three samples Nos. (3)–(5) (see Fig. 5, where an example for the two separate components, $I_{\mathrm{coh}}(q)$ and $I_{\mathrm{inc}}(q)$, is also reported).

IV. DISCUSSION

Once the fully processed neutron scattering spectra, $I_E(q,\omega)$, for samples Nos. (3)–(5) have been obtained, the first issue to be tackled was their normalization, since each data set contained an unknown instrumental constant N_e (making a total of six values considering three samples and the two E_i options) such that $I_E(q,\omega) = N_e I(q,\omega)$. To this aim, the knowledge of the simulated neutron scattering structure factors, $I(q)$, was exploited. However, dealing with the two mixtures, some caution was needed, since the ω-integrated incoherent component, $I_{\mathrm{inc}}(q)$, containing D_2 rotovibrational contributions, might extend well beyond the spectral range probed by our neutron measurements, especially at large q values. In order to circumvent this problem, individual $I_{\mathrm{inc}}(q,\omega)$ spectra were simulated using CMD in conjunction with the Gaussian approximation and integrated in the ω range actually accessible to the spectrometer. Using this approach, a better agreement between experimental and simulated data has been obtained (see Fig. 5 for data with $E_i = 40.0$ meV) allowing for a reliable data normalization procedure. Subsequently, for samples Nos. (4) and (5), the $I_{\mathrm{inc}}(q,\omega)$ contributions were subtracted from the normalized experimental spectra, giving rise to experimental estimates of $I_{\mathrm{coh}}(q,\omega)$, dubbed $I_{\mathrm{coh}}^{(E)}(q,\omega)$ in what follows.
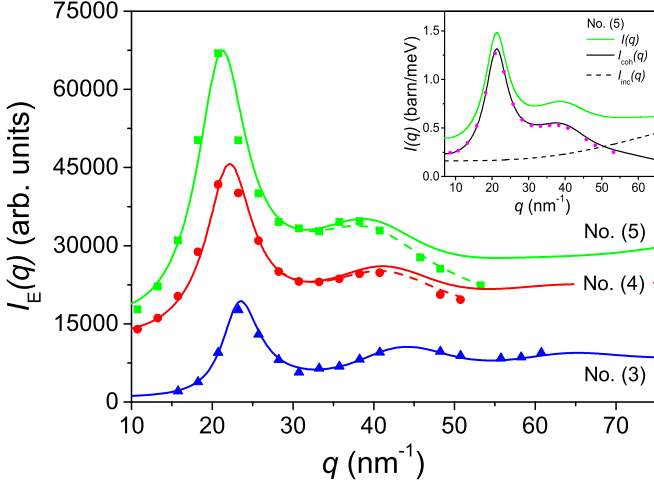
FIG. 5. The ω-integrated experimental spectra, $I_E(q)$, reported as solid symbols, together with the corresponding PIMC-simulated neutron structure factors, $I(q)$, multiplied for appropriate scale factors (full lines). Data associated to sample No. (3) are plotted in blue with triangles, those to sample No. (4) are plotted in red with circles, and those to sample No. (5) are plotted in green with squares. Dashed lines show that at high q values the D_2 incoherent component extends out of the experimentally accessible ω range (see the main text for details). In the inset the PIMC-simulated neutron structure factor, $I(q)$, for sample No. (5) is divided into its two components: coherent, $I_{coh}(q)$, and incoherent, $I_{inc}(q)$. In addition, the RPMD evaluation of $I_{coh}(q)$ is also reported as magenta dots.

A. Comparison between experimental and simulated coherent spectra

Prior to a physical analysis of the coherent spectra [both experimental $I_{coh}^{(E)}(q, \omega)$ and simulated $I_{coh}(q, \omega)$], it is worthwhile to establish a direct comparison between these two groups of data sets, starting from the simple case of pure neon which corresponds to the experimental sample No. (3) (see Table I), and to simulations Nos. (i) and (I) (see Table II) for FK-LPI–FK-QCW and RPMD, respectively. Constant-q coherent experimental spectra taken at $E_i = 40$ meV are compared, for selected wave-vector transfer values, with the results of FK-LPI, FK-QCW, and RPMD simulations in Fig. 6. Although the agreement between neutron scattering data and quantum simulations is globally quite good for all three techniques, one can notice that it slightly worsens as q increases beyond 35–40 nm^{-1}. In addition, a comparison among the simulated data shows that RPMD seems to perform better than FK-QCW in the high-q spectral region, while FK-LPI behaves in this region definitely better than the other two methods, as revealed by an analysis of the reduced chi-square (χ_r^2) values: Averaging χ_r^2 values for $q > 45$ nm^{-1}, one finds $\overline{\chi_r^2} \simeq 1.50$ (FK-LPI) to be compared with $\overline{\chi_r^2} \simeq 3.63$ (RPMD) and 9.48 (FK-QCW).

A careful inspection of the three simulated spectra showed that the main reason of this different high-q behavior is related to the spectral recoil and the first-moment sum rule [7] which, as we have mentioned earlier, is exactly reproduced by the FK-LPI technique. Nevertheless, the advantage of RPMD
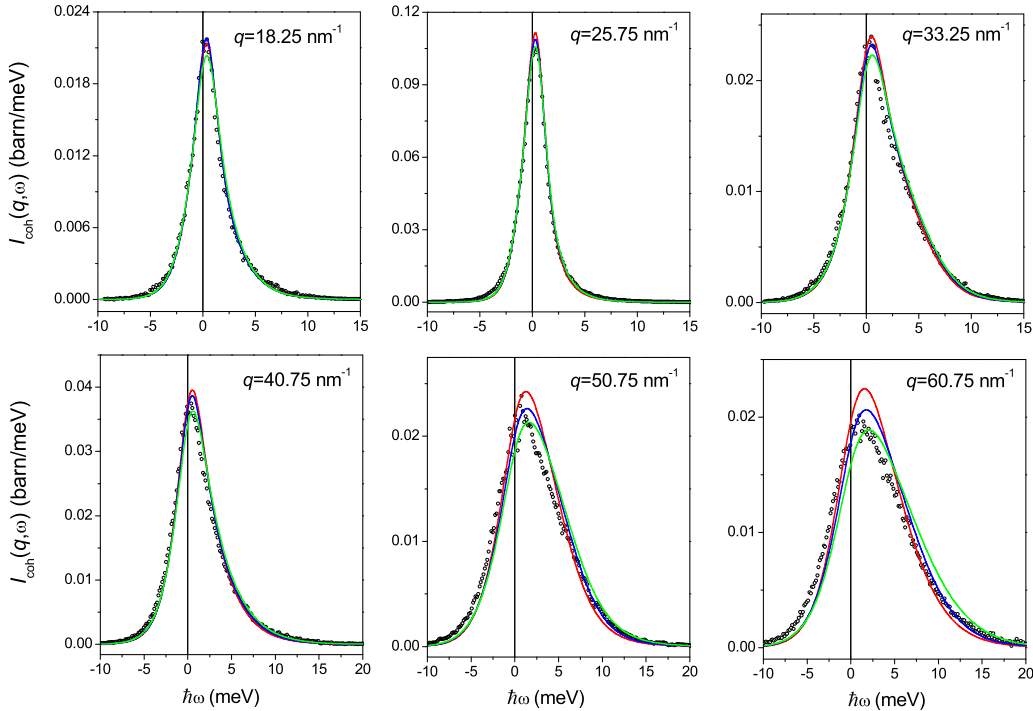

FIG. 6. Coherent experimental spectra, $I_{coh}^{(E)}(q, \omega)$, from sample No. (3), pure Ne, for $E_i = 40.0$ meV are reported for selected q values as black empty circles. Corresponding simulated data, $I_{coh}(q, \omega)$ (see main text for details) are plotted as lines: blue for RPMD, green for FK-LPI, and red for FK-QCW.

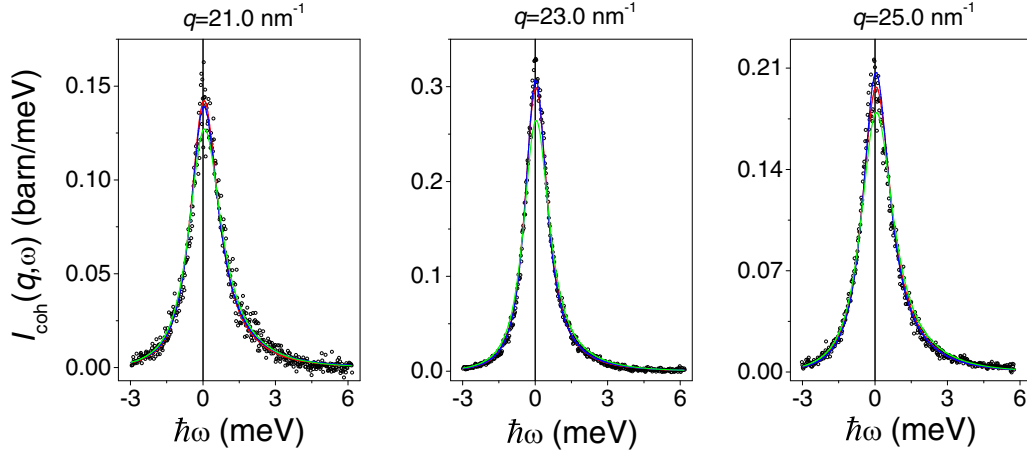FIG. 7. Coherent experimental spectra, $I_{coh}^{(E)}(q, \omega)$, from sample No. (3), pure Ne, for $E_i = 7.1$ meV are reported for selected q values as black empty circles. Corresponding simulated data, $I_{coh}(q, \omega)$ (see main text for details) are plotted as lines: blue for RPMD, green for FK-LPI, and red for FK-QCW.

over FK-QCW is somehow unexpected, since, as we have mentioned above, the former method should be used mainly for low values of q, surely not for those beyond the first minimum of the static structure factor. For example, in pure liquid deuterium it has been recently verified that the RPMD $F_{D_2,D_2}(q, 0)$ compares well with the PIMC $S_{D_2,D_2}(q)$ up to $q = 20$ nm^{-1}, as shown in Fig. 4 of Ref. [10]. However, our positive findings about RPMD simulations might be explained by the fact that the spectra used in the present context have been corrected for the shortcomings of such a simulation technique to produce accurate static structure factors (at medium and high values of q) by applying scaling constants to the various spectra in order to reproduce the corresponding PIMC results. The magnitude of this effect can be easily appreciated in the inset of Fig. 5. An analogous spectral comparison for the same sample, but measured at $E_i = 7.1$ meV (and so exhibiting better energy transfer resolution but worse statistical accuracy), is presented in Fig. 7 and, although spanning a narrower q range, confirms the good agreement between neutron scattering data and quantum simulations reported above. However, in this case, which is related to the region roughly corresponding to the so-called *de Gennes narrowing* [41], FK-LPI seems to perform slightly worse than the other two methods, since $\overline{\chi}_r^2 \simeq 1.46$ (FK-LPI) is larger than $\overline{\chi}_r^2 \simeq 1.02$ (FK-QCW) and 0.98 (RPMD), averaging χ_r^2 over the 21 nm^{-1} $< q <$ 27 nm^{-1} range.

Moving to the low D_2-concentration mixture, namely sample No. (4), we have reported constant-q coherent experimental spectra taken at $E_i = 40.0$ and 7.1 meV in Figs. 8 and 9, respectively. Here neutron scattering data are again compared, for selected wave-vector transfer values, with the results of FK-LPI, FK-QCW, and RPMD simulations. However, differently from the pure neon case, the agreement between the experiment on one side and the last two quantum simulations on the other is not always completely satisfactory, both at low q and high q values, while in the intermediate wave-vector transfer region [i.e., close to the first maximum of $I_{coh}(q)$] it is reasonably good. As for the differences between the FK-QCW and RPMD results, like in the previous case, they are negligible at low q values, becoming more

pronounced for $q > 30$ nm^{-1}, where, quite unexpectedly, the latter technique seems to behave slightly better than the former as far as the agreement with the neutron scattering data is concerned: $\overline{\chi}_r^2 \simeq 22.76$ (FK-QCW) compared with $\overline{\chi}_r^2 \simeq 13.19$ (RPMD).

On the other hand, FK-LPI provides the best description of the neutron data taken at $E_i = 40.0$ meV, except in the region roughly corresponding to the de Gennes narrowing (namely, 18 nm^{-1} $< q <$ 24 nm^{-1}), where the spectra are expected to shrink. Here FK-QCW and RPMD outperform FK-LPI, as already visible in Fig. 8 and clearly confirmed by the experimental spectra taken with $E_i = 7.1$ meV in Fig. 9, since the FK-LPI peaks appear slightly too broad. Here, averaging χ_r^2 over the 18 nm^{-1} $< q <$ 26 nm^{-1} range, one observes $\overline{\chi}_r^2 \simeq 2.41$ (FK-LPI), to be contrasted with $\overline{\chi}_r^2 \simeq 1.87$ (RPMD) and 1.84 (FK-QCW).

Dealing with the high D_2-concentration mixture, namely sample No. (5), we have plotted constant-q coherent experimental spectra taken at $E_i = 40.0$ and 7.1 meV in Figs. 10 and 11, respectively, together with the corresponding RPMD, FK-LPI, and FK-QCW simulations. Although the larger amount of D_2 with respect to sample No. (4) has the effect of substantially broadening all the spectral features, the qualitative trends of the comparison between experiment on one side, and RPMD, FK-LPI, and FK-QCW on the other, are totally confirmed: The agreement between experimental spectra and RPMD data is not always completely satisfactory, both at low q and high q values, while at intermediate wave-vector transfers, close to the first maximum of $I_{coh}(q)$, it is good. On the contrary, FK-LPI is superior both at low q and high q values, but it shows some discrepancies in the region near the de Gennes narrowing up to about $q = 25$ nm^{-1}. For example, averaging χ_r^2 for $q > 30$ nm^{-1}, one observes that $\overline{\chi}_r^2 \simeq 8.25$ for this technique and about 42.28 for RPMD (at $E_i = 40.0$ meV). As for FK-QCW, at low q values its spectra are almost indistinguishable from the RPMD ones, while increasing the wave-vector transfer a certain lack of recoil becomes evident and the former technique performs rather poorly.
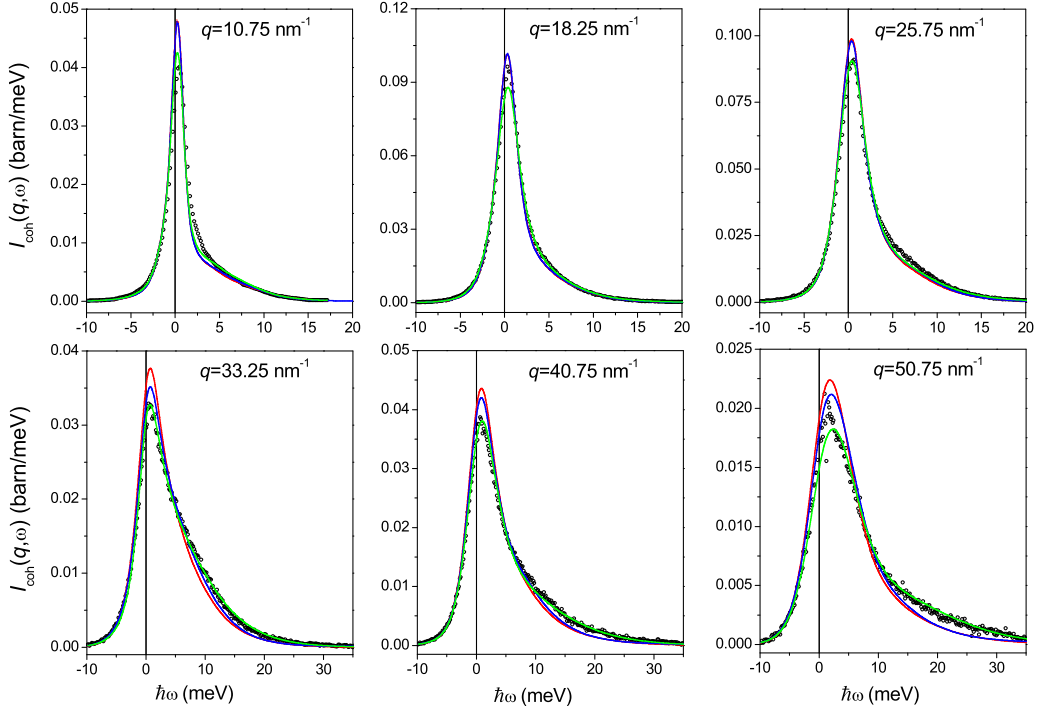
FIG. 8. Coherent experimental spectra, $I_{coh}^{(E)}(q, \omega)$, from sample No. (4), low D_2-concentration mixture, for $E_i = 40.0$ meV are reported for selected q values as black empty circles. Corresponding simulated data, $I_{coh}(q, \omega)$ (see main text for details) are plotted as lines: blue for RPMD, green for FK-LPI, and red for FK-QCW.

B. Further spectral analysis: Longitudinal current-current time correlation functions

A further analysis of the mentioned coherent spectra, both experimental and simulated, can be performed through the study of the *longitudinal current-current time correlation* (LC-CTC) function [41] and its spectrum, $\tilde{c}_L(q, \omega)$, which can provide some approximate, although quite useful, information on the dispersion of collective excitations in disordered systems. This task is accomplished by investigating the ω position of the maximum of $\tilde{c}_L(q, \omega)$ and its variation with q, where the LCCTC spectrum is simply proportional to ω^2

times the scattering law (even in quantum systems [42]):

$$\tilde{c}_L(q, \omega) = \frac{\omega^2}{q^2} S(q, \omega). \tag{11}$$

This formula can be easily implemented in the case of sample No. (3), consisting of pure neon, both for simulated (i.e., RPMD, FK-QCW, and FK-LPI) and experimental data. The latter are reported in Fig. 12 for some selected values of q. Results for the LCCTC spectrum analysis are shown in Fig. 13 where the ω maxima of $\tilde{c}_L(q, \omega)$, dubbed Ω_d, are reported as a function of q, giving rise to various dispersion curves of $\Omega_d(q)$ (named simply "dispersion curves" in the rest of the
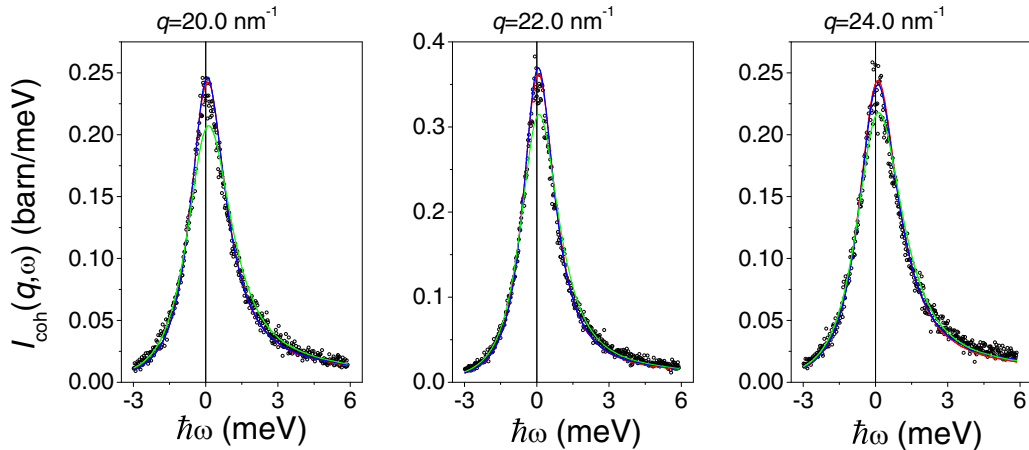

FIG. 9. Coherent experimental spectra, $I_{coh}^{(E)}(q, \omega)$, from sample No. (4), low D_2-concentration mixture, for $E_i = 7.1$ meV are reported for selected q values as black empty circles. Corresponding simulated data, $I_{coh}(q, \omega)$ (see main text for details) are plotted as lines: blue for RPMD, green for FK-LPI, and red for FK-QCW.
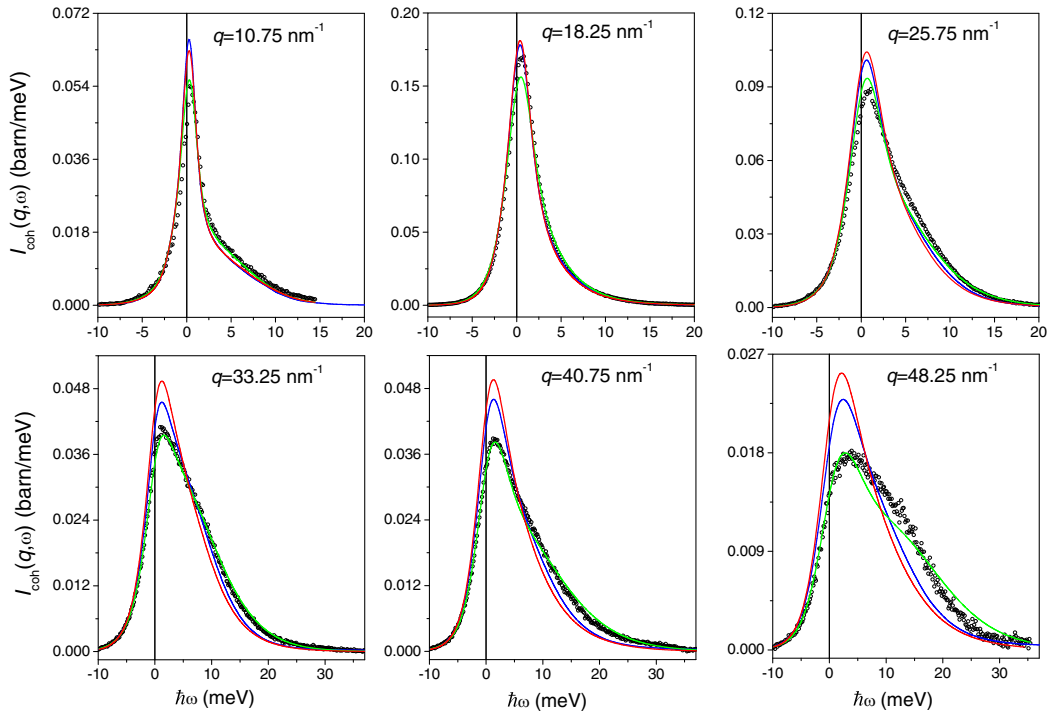
FIG. 10. Coherent experimental spectra, $I_{coh}^{(E)}(q, \omega)$, from sample No. (5), high D_2-concentration mixture, for $E_i = 40.0$ meV are reported for selected q values as black empty circles. Corresponding simulated data, $I_{coh}(q, \omega)$ (see main text for details) are plotted as lines: blue for RPMD, green for FK-LPI, and red for FK-QCW.

paper). These curves exhibit the typical behavior of a simple liquid, and the agreement among the three simulated data sets is generally good even though it slightly deteriorates at high q values, where, not surprisingly considering what we have seen above, the RPMD dispersion curve lies in between those from FK-QCW and FK-LPI. As for the neutron scattering $\Omega_d(q)$, one can observe that the corresponding dispersion curve is satisfactorily described by the simulated ones, especially by the FK-LPI curve which correctly reproduces the high-q trend, too. In this respect, it is worth noting that all these four LCCTC spectra, $\tilde{c}_L(q, \omega)$, are evaluated directly via

Eq. (11) from the respective Ne dynamic structure factors. But while the three simulated $S_{Ne,Ne}(q, \omega)$ are directly the Fourier transforms of the quantum technique outputs exhibiting only a minute ω broadening (due to the finite time cutoff on the simulated correlation functions), the neutron scattering LCCTC spectra show a different situation: The experimental dynamic structure factors actually contain a convolution with the instrumental energy resolution function, as shown in Eq. (6), which does not commute with the product with ω^2. In other words, the experimental resolution-broadened dynamic structure factor, strictly speaking, does not give rise to an
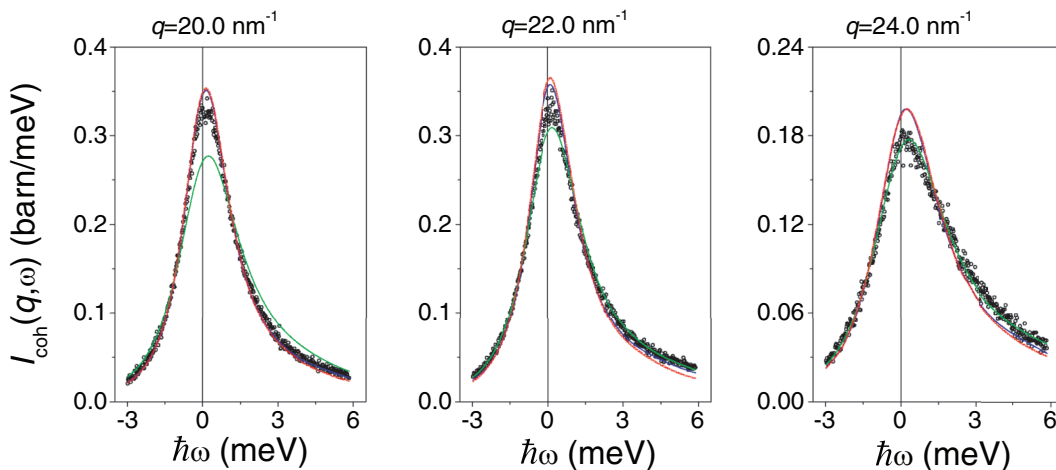

FIG. 11. Coherent experimental spectra, $I_{coh}^{(E)}(q, \omega)$, from sample No. (5), high D_2-concentration mixture, for $E_i = 7.1$ meV are reported for selected q values as black empty circles. Corresponding simulated data, $I_{coh}(q, \omega)$ (see main text for details) are plotted as lines: blue for RPMD, green for FK-LPI, and red for FK-QCW.
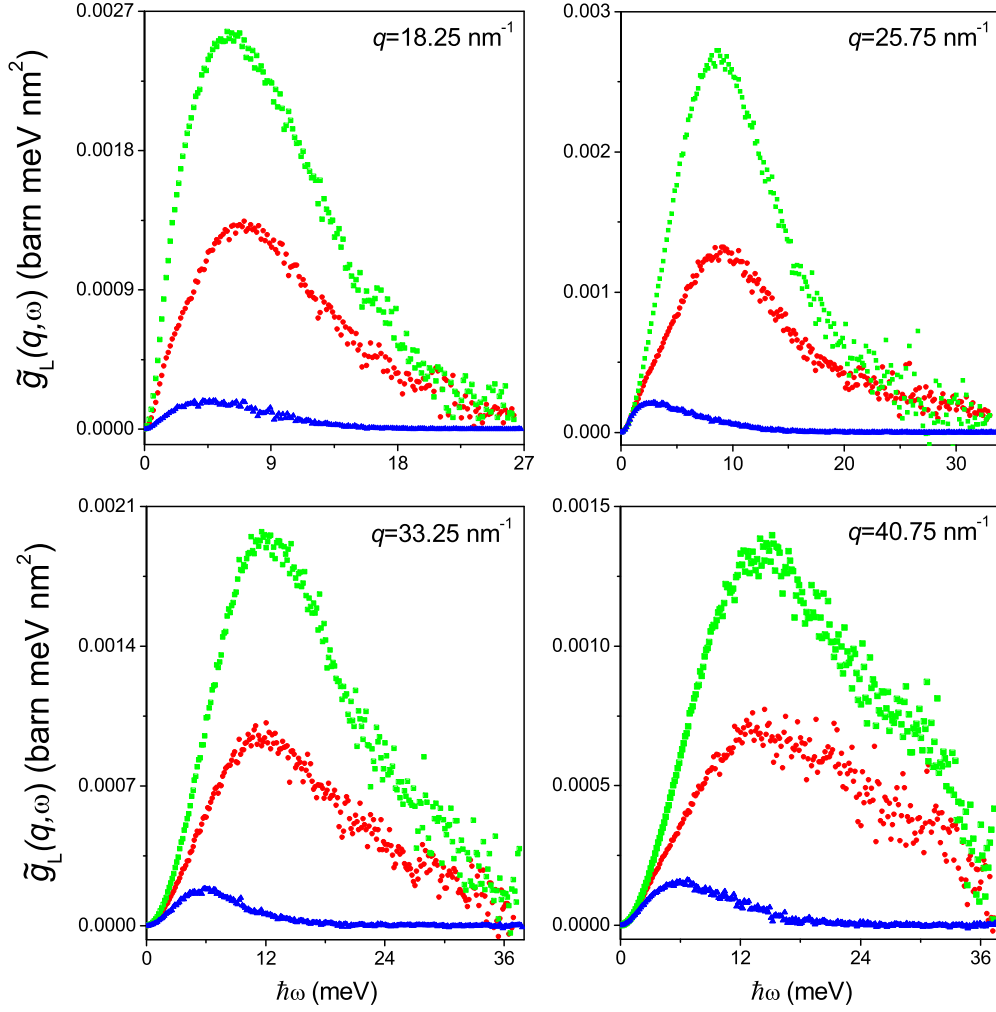
FIG. 12. Generalized longitudinal current-current time correlation spectra, $\tilde{g}_L(q,\omega)$, derived from experimental neutron data with $E_i = 40.0$ meV, are reported for selected q values as follows: blue triangles for sample No. (3), red circles for sample No. (4), and green squares for sample No. (5). In the first case, related to pure Ne, $\tilde{g}_L(q,\omega)$ coincides with the standard longitudinal current-current time correlation spectrum, $\tilde{c}_L(q,\omega)$.

exact resolution-broadened $\tilde{c}_L(q,\omega)$, especially in the case of $E_i = 40.0$ meV, where the broadening is larger. However, as suggested by the results plotted in Fig. 13, it seems that this effect is not relevant in the present context. The hydrodynamic low-q behavior of $\Omega_d(q)$, obtained from the speed of sound data reported in Ref. [16](namely, $c = 544.5$ m/s) is also plotted in Fig. 13, where one can observe a fairly good matching between simulations and hydrodynamic slope, even though there is no evidence of positive dispersion, which in liquid neon [43] is to be expected. However, as pointed out earlier, the study of the liquid Ne and Ne-D_2 hydrodynamics is outside the scope of the present work, and so we are not going to further discuss this point.

Moving to the two D_2-Ne mixtures, namely samples Nos. (4) and (5), one has to notice that Eq. (11) must be modified

as follows:

$$\tilde{c}_L(q,\omega) = \frac{\omega^2}{q^2} \sum_{\alpha=1}^{2} \sum_{\beta=1}^{2} S_{\alpha,\beta}(q,\omega), \tag{12}$$

where α and β can represent either a Ne atom or a D_2 center of mass. However, this formula is applicable only to the simulated spectra since the experimental ones appear in the form of Eq. (6), where the partial components are weighted by the respective neutron cross sections and lumped together. So, in the neutron scattering case, the only accessible quantity is the *generalized longitudinal current-current time correlation* spectrum, $\tilde{g}_L(q,\omega)$, which includes in its definition the appropriate neutron scattering lengths:

$$\tilde{g}_L(q,\omega) = \left(\frac{\omega}{q}\right)^2 \frac{(b_c[\text{Ne}])^2 S_{\text{Ne,Ne}}(q,\omega) + 2b_c[\text{Ne}]\sqrt{u(q)}S_{\text{Ne},D_2}(q,\omega) + u(q)S_{D_2,D_2}(q,\omega)}{(b_c[\text{Ne}])^2 + 2b_c[\text{Ne}]\sqrt{u(q)} + u(q)}. \tag{13}$$
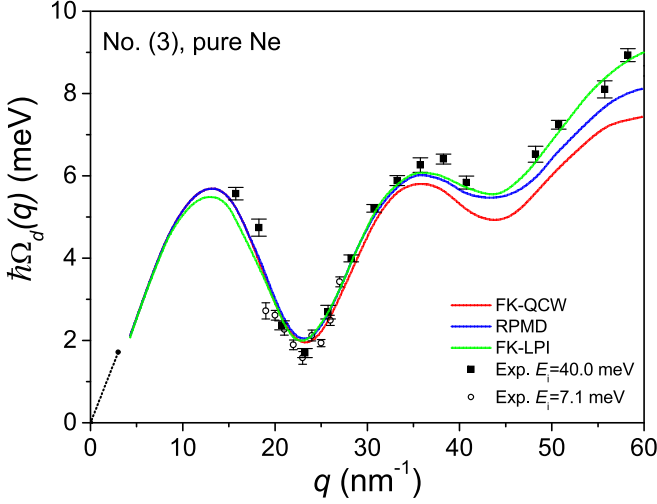
FIG. 13. Dispersion curves $\Omega_d(q)$ derived from the positions of the maxima of the longitudinal current-current time correlation spectra, $\tilde{c}_L(q, \omega)$, obtained according to Eq. (11) in the case of sample No. (3), i.e., pure Ne. Red line represents $\Omega_d(q)$ for the FK-QCW simulated spectra, while blue and green lines stand for the dispersion curves from RPMD and FK-LPI, respectively. As for the experimental results, full squares (with error bars) are derived from neutron scattering data measured with $E_i = 40.0$ meV, and empty circles (with error bars) from those measured with $E_i = 7.1$ meV. The hydrodynamic low-q behavior from speed of sound data in Ref. [16] is also represented as a black dotted straight line.

Obviously, in the case of pure Ne $\tilde{c}_L(q, \omega)$ and $\tilde{g}_L(q, \omega)$ coincide. From the various estimates of $\tilde{g}_L(q, \omega)$, including RPMD, FK-QCW, FK-LPI, and neutron data with $E_i = 40.0$ meV (see Fig. 12 for the last technique), it is still possible to study the ω position of the maximum of each generalized LCCTC spectrum and its variation with q, in order to determine the corresponding six pseudodispersion curves $\Omega_{pd}(q)$, reported in Fig. 14. One can immediately note that, once a technique is selected (either RPMD, or FK-QCW, or FK-LPI, or neutron scattering), the similarity between the data sets belonging to the two different mixtures is striking. Moreover, and not surprisingly due to the larger neutron scattering visibility of D_2 with respect to Ne, the $\Omega_{pd}(q)$ curves appear rather dissimilar from the neon dispersion curve derived from the maxima of $\tilde{c}_L^{(l)}(q, \omega)$ (see Fig. 13). As for the comparisons among the RPMD, FK-QCW, FK-LPI, and neutron scattering $\Omega_{pd}(q)$ curves, one can observe that these are less satisfactory than in the pure Ne case and, as expected from what has been found in Sec. IV A, worsen at high q values. However, it is also worth noticing that the experimental $\Omega_{pd}(q)$ curves often lie in between the RPMD and the FK-LPI ones, while the FK-QCW results are hardly distinguishable from those derived from RPMD.

Going back to Eq. (12), one could in principle extract the plain $\Omega_d(q)$ from the quantum simulation results for samples Nos. (4) and (5). However, one immediately realizes that these dispersion curves turn out to be quite different from the pure Ne case, as the $\tilde{c}_L(q, \omega)$ spectra often appear broad or strongly asymmetric and, sometimes, they even show a bimodal character with a main peak preceded (or, more rarely, followed) by
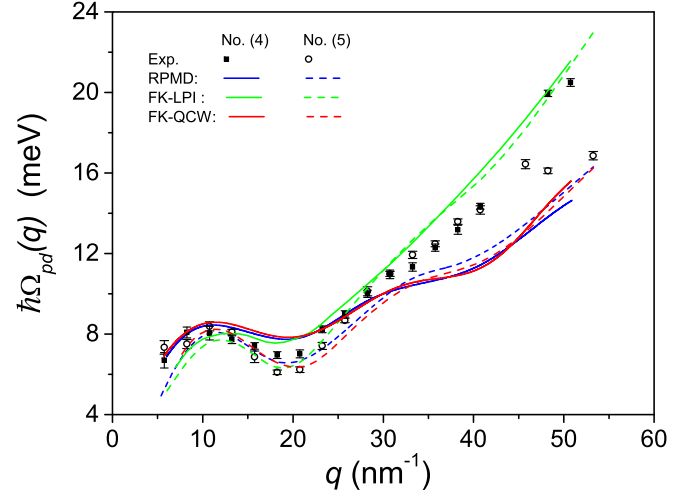

FIG. 14. Pseudodispersion curves, $\Omega_{pd}(q)$, derived from the positions of the maxima of the generalized longitudinal current-current time correlation spectra, $\tilde{g}_L(q, \omega)$, obtained according to Eq. (13) in the case of sample No. (4) (full lines and full squares with error bars) and No. (5) (dashed lines and empty circles with error bars). Blue lines represent curves from the RPMD simulated spectra, green and red lines stand for those from FK-LPI and FK-QCW, respectively, while symbols with error bars stand for the corresponding experimental results measured with $E_i = 40.0$ meV.

a smaller one. All these findings reveal the presence of more than one contribution to the LCCTC, as clearly pointed out by González *et al.* [44] in the analysis of their simulations of Li-Na liquid mixtures, where three distinct components of $\tilde{c}_L(q, \omega)$ have been identified. Thus, also in our case, where the mass ratio D_2-Ne is even larger than the Li or Na one, all the three LCCTC components,

$$\tilde{c}_{L\alpha,\beta}(q, \omega) = \frac{\omega^2}{q^2} S_{\alpha,\beta}(q, \omega), \tag{14}$$

will be required. Needless to say, $\tilde{c}_{L\alpha,\beta}(q, \omega)$ always coincides with $\tilde{c}_{L\beta,\alpha}(q, \omega)$. Naturally, these three contributions could be separately studied and their respective maxima extracted as a function of q and $x[D_2]$. However, the cross terms in Eq. (14), i.e., those with $\alpha \neq \beta$, are not positive functions of ω, and so the positions of their extrema might be misleading. For this reason, it is more convenient to reduce the number of distinct contributions to the LCCTC of samples Nos. (4) and (5) by attributing them to the lightweight masses, $\tilde{c}_L^{(l)}(q, \omega)$, and the heavy masses, $\tilde{c}_L^{(h)}(q, \omega)$, according to the following scheme:

$$\tilde{c}_L^{(l)}(q, \omega) = \frac{\omega^2}{q^2} \left\{ S_{D_2,D_2}(q, \omega) + 2x[D_2]S_{Ne,D_2}(q, \omega) \right\},$$

$$\tilde{c}_L^{(h)}(q, \omega) = \frac{\omega^2}{q^2} \left\{ 2x[Ne]S_{Ne,D_2}(q, \omega) + S_{Ne,Ne}(q, \omega) \right\}, \tag{15}$$

with the former dominated by the D_2 centers of mass and the latter by the Ne atoms. The partial-LCCTC maxima analysis in terms of lightweight and heavy masses is summarized in Fig. 15, where the effects of the Ne-D_2 mixing on the $\Omega_d(q)$ curves are clearly highlighted through a comparison with the RPMD simulations of the two pure liquid systems.
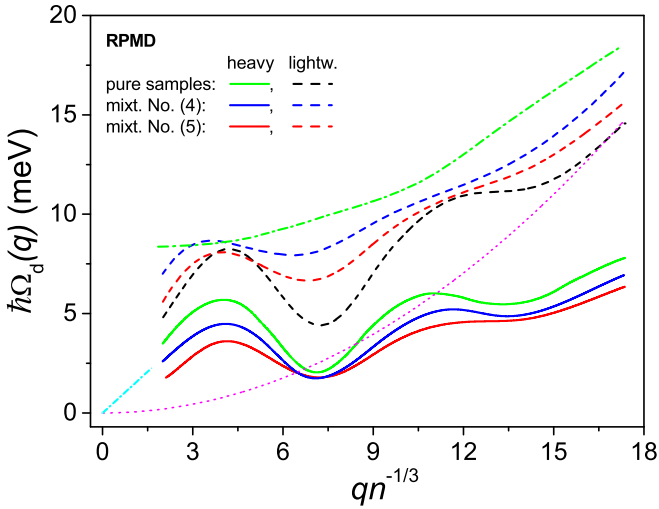
FIG. 15. Position of the maxima of the lightweight, $\tilde{c}_L^{(l)}(q, \omega)$, and heavy, $\tilde{c}_L^{(h)}(q, \omega)$, longitudinal current-current time correlation spectra from RPMD simulations are reported as dashed lines and full lines, respectively. Both types of red lines are related to sample No. (5), both types of blue lines to sample No. (4); while the green full line refers to sample No. (3) and the black dashed line to pure liquid D_2 [i.e., simulation No. (VIII) in Table II]. The adimensional physical quantity on the abscissa is the reduced wave-vector transfer, $qn^{-1/3}$. The green dot-dashed line is the limiting $\tilde{c}_L^{(l)}(q, \omega)$ in case of an infinite D_2 dilution (see main text for details), while the magenta dotted line represents the free recoil of the D_2 center of mass evaluated for the density of sample No. (4). The hydrodynamic low-q behavior from speed of sound data in Ref. [16] is also represented as a cyan dot-dashed straight line for sample No. (4), which almost coincides with the corresponding estimate for sample No. (5).

In order to make this comparison more straightforward, we have replaced q with the adimensional reduced wave vector $qn^{-1/3}$, which corrects for the density changes induced by varying the concentration $x[D_2]$. As for the heavy-mass component, one sees a gradual reduction of the frequency values as the deuterium concentration grows and the system expands, together with a modest change in the dispersion curve shape with peaks and troughs becoming slightly less pronounced. These findings, mainly related to the Ne atoms dynamics, are not surprising and can be easily explained by the system density changes from $n = 24.8$ nm^{-3} [i.e., sample No. (5)] up to $n = 34.4$ nm^{-3} [i.e., sample No. (3)], as shown in Table I. On the contrary, for the lightweight-mass component, the modifications induced by the presence of Ne look more relevant and the corresponding $\Omega_d(q)$ curves depart from the pure D_2 case in a substantial way, to such an extent that in sample No. (4) the first minimum of the dispersion curve is barely visible, revealing some resemblance to an opticlike mode. However, as $qn^{-1/3}$ grows larger than 12-13, the two mixture lightweight-mass dispersion curves seem largely dominated by the D_2 center-of-mass recoil and exhibit a typical parabolic trend, which is usually associated with an (almost) free-particle dynamics. As for the overall frequency magnitudes of the lightweight-mass dispersion curves, these, too, follow the system density changes from $n = 21.4$ nm^{-3} (i.e., pure D_2) up to $n = 28.9$ nm^{-3} [i.e., sample No. (4)], as

shown in Tables I and II. The hydrodynamic low-q behavior of $\Omega_d(q)$, obtained interpolating the scanty data for the Ne-D_2 speeds of sound contained in Ref. [16], is also plotted in Fig. 15 for both samples No. (4) and (5), which actually turned out to be hardly distinguishable from each other: $c = 429.6$ and 422.6 m/s, respectively. Unsurprisingly, one can observe a good matching between the heavy-mass component simulation and the hydrodynamic slope, at least as far as sample No. (4) is considered, even though, similarly to the pure Ne case, no positive dispersion is detectable in our data.

At this stage it is possible to set up a comparison between the present findings for the $\Omega_d(q)$ of the lightweight masses, a direct expression of the deuterium collective dynamics, and the aforementioned CMD spectra of the velocity autocorrelation function, $f_{D_2}(\omega)$, which, on the contrary, are related to the self-dynamics of the D_2 centers of mass contained in the liquid mixtures. However, before doing so, it is important to bear in mind some subtle differences between lightweight-mass $\Omega_d(q)$ and $f_{D_2}(\omega)$, which are less obvious than the simple contrast between collective and single-particle dynamics. The former physical quantity also contains, as clearly shown in Eq. (15), a part which is due to the dynamic interplay between D_2 and Ne and, moreover, extends over a large q range so that it cannot be simply understood as the dispersion of the single longitudinal pseudophonons present in the system. In this context, it is useful to define the *first pseudo-Brillouin zone* of the liquid system, as a sphere whose radius is roughly given by $q_{sdp}/2$, with q_{sdp} being the wave-vector transfer value pertaining to the so-called *first sharp diffraction peak* of the static structure factor. In our case, looking at the reported PIMC results, one can assume the following values for q_{sdp}: 22.59 and 21.72 nm^{-1} for samples No. (4) and No. (5), respectively, and beyond the center of the second pseudo-Brillouin zone (i.e., for $q > q_{sdp}$) the dispersion curve will not be considered for the present comparison. On the other hand, as far as the latter physical quantity is concerned, it is well known that $f_{D_2}(\omega)$ is defined in such a way as to contain only single pseudophononic components, since it can be also conceived as an appropriate $q \rightarrow 0$-limit of the self-scattering law [7]. However, $f_{D_2}(\omega)$, differently from all the physical quantities related to the LCCTC, is fully insensitive to the difference between longitudinal and transverse dynamics, encompassing both types of pseudophonons. So, considering that in a simple fluid the transverse dynamics exhibits lower frequencies than those related to the longitudinal one, it is to be expected that the low-ω part of $f_{D_2}(\omega)$ will have an excess of modes having no counterpart in $\Omega_d(q)$. In addition, around $\omega = 0$, the LCCTC spectrum contains traces of the diffusive modes which, needless to say, are completely absent in a dispersion curve. With these clarifications, we can now return to the CMD spectra, i.e., $f_{D_2}(\omega)$ and $f_{Ne}(\omega)$, for samples Nos. (3)–(5), as well as pure D_2 [namely, simulation No. (VIII) in Table II], all reported in Fig. 16. In Fig. 16(a) one can observe the variation of $f_{Ne}(\omega)$ with the density of the system which changes from $n = 34.4$ nm^{-3} [i.e., sample No. (3)] to $n = 24.8$ nm^{-3} [i.e., sample No. (5)] due to the presence of deuterium. The frequency distribution gets clearly red shifted and the Ne self-diffusion coefficient, $D_{s,Ne}$, which is proportional to $f_{Ne}(0)$ [32], grows in a significant way. These findings are not unexpected and confirm the results of the dispersion curve
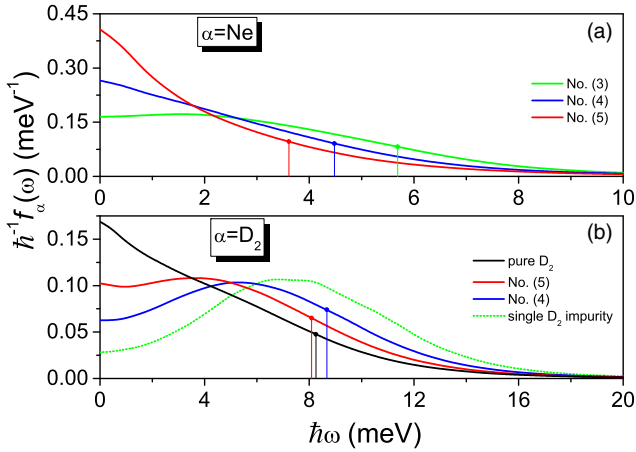
FIG. 16. Spectra of the CMD velocity autocorrelation functions for Ne atoms (a) and D_2 centers of mass (b). Blue and red full lines represent simulations for samples Nos. (4) and (5), respectively; while the black full line stands for the pure D_2 case [i.e., No. (VIII) in Table II]. As for the green lines, which are related sample No. (3), the full one is the pure Ne contribution, while the dotted one is the infinite-dilution spectrum of a single D_2 impurity in neon. Vertical sticks mark the positions of the first maximum of the various $\hbar\Omega_d$ curves reported in Fig. 15.

analysis of Fig. 15, now shown by the vertical sticks which mark the positions of the first maximum of the Ω_d curves. As for the $f_{D_2}(\omega)$ distributions plotted in Fig. 16(b), one can observe, along with density effects similar to those visible in Fig. 16(a), an important modification of the spectral shape, which gradually becomes less liquidlike (i.e., monotonically decreasing at zero frequency) and more solidlike (i.e., exhibiting a marked hump) as the total molecular number density n increases, up to the infinite-dilution spectrum of a single D_2 impurity in neon, which has been extrapolated from the CMD simulations reported in Table II and shows a large mean kinetic energy value: $\langle E_K \rangle_{D_2} = (78 \pm 1)$ K. However, differently from the Ne case, the vertical stick positions here are not much affected by the system density. One should note that this liquidlike to solidlike transition is in perfect agreement with the H_2 behavior in Ne-H_2 mixtures, recently investigated via incoherent neutron scattering and quantum simulations, which have been described in detail in Ref. [9].

Finally, considering that in the case of an infinite D_2 dilution, the lightweight-mass $\tilde{c}_L^{(l)}(q, \omega)$ in Eq. (15) simply coincides with its D_2 self-component, $\omega^2 q^{-2} S_{s,D_2}(q, \omega)$, one can exploit the mentioned extrapolated CMD spectrum, in conjunction with the Gaussian approximation, in order to extract the corresponding dispersion curve, reported in Fig. 15. This line represents a sort of limiting case for the Ne/D_2 mixtures as the deuterium concentration decreases and the system becomes denser and denser. Naturally, the typical oscillating structure of $\Omega_d(q)$ disappears and the smooth growing trend with q reveals the progressively increasing role played by the single particle recoil in $S_{s,D_2}(q, \omega)$. It is worth noting that the D_2 center-of-mass dynamics in an infinitely diluted system is approximately described by the quantum version of the well-known *itinerant oscillator* model, which has been studied in detail in the past by various authors [45].

V. CONCLUSIONS

In this study we have presented new and original neutron scattering spectra of normal deuterium mixed with liquid neon (at a temperature $T = 30.0$ K) for three values of the D_2 molar concentration (i.e., $x[D_2] = 0\%$, 23%, and 49%), using the neutron chopper spectrometer MARI [12] with two different incoming energy values: $E_i = 40.0$ and 7.1 meV. These double-differential neutron scattering cross sections were supposed to provide experimental information on the collective dynamics of the centers of mass for the two species in the aforementioned liquid samples. In order to fulfill this task, neutron scattering data were corrected for the standard experimental effects (e.g., empty cell signal, self-shielding, multiple scattering), and the incoherent scattering contributions were subtracted, including those from the rotovibrational D_2 dynamics, carefully estimated in the framework of the modified Young and Koppel model [24,25] and in conjunction with the Gaussian approximation [32]. After carrying out this procedure, we obtained an approximate mapping of the mixture scattering laws in the wave-vector transfer range 4 nm$^{-1} < q < 51$ nm^{-1}, and in the energy transfer range -10 meV $< \hbar\omega < 38$ meV. Molecular dynamics calculations, performed with three different approximate quantum simulation methods, such as RPMD [27] and two variants of the Feynman-Kleinert approach (namely, FK-QCW [29] and FK-LPI [28]) provided spectra of the same physical quantities derived from the neutron measurements. In addition, similarly to the previously studied case of Ne-H_2 mixtures [9], accurate estimates of the velocity autocorrelation function for D_2 centers of mass, as well as for Ne atoms, were produced using a fourth approximate quantum simulation method, CMD [26], and contained valuable physical information which was also used as an input to the mentioned Gaussian approximation calculations. The general agreement among experimental spectra and the various simulation results was largely satisfactory for the pure Ne sample, while, as far as the D_2 presence is concerned, some discrepancies both among simulations, and between simulations and experimental data, could be detected. In particular, in terms of capabilities to reproduce neutron scattering data, FK-QCW seems to be a less well-performing method overall, while RPMD is the best in the intermediate q region (roughly corresponding to the de Gennes narrowing zone [41]), and FK-LPI produces excellent spectra in the high-q region, where the D_2 recoil is already relevant. Although it is difficult to generalize the results of the present study to other disordered systems exhibiting sizable quantum effects, it seems that we are now in a position to add some information why certain simulation techniques are more satisfactory in a given q range than in other intervals. As a comparison with the PIMC reference data shows, FK-LPI and FK-QCW are both able to correctly reproduce the static structure at all q values. In general, this cannot be rigorously expected and depends on the system and the range of wave vectors considered. Due to the exponential "weight factor" in Eq. (18) of Ref. [46] or Eq. (38) of Ref. [35], which contains terms linear and quadratic in q, the static structure factor given by $F_{\alpha,\beta}(q, 0)$ will drop below its asymptotic value of 1 and eventually fall to zero for extremely large q values. Whether this becomes noticeable in the range of experimental

wave numbers will depend on the system and the thermodynamic conditions, but surely not in the present context of liquid Ne and Ne-D_2 mixtures. On the other hand, FK-LPI is guaranteed to also reproduce the recoil term because its correct value is built into the algorithm [46]. By contrast, RPMD, at least in its raw form, fails to estimate the static structure at high q values where, in addition, also the recoil term turns out to be underestimated. However, if each RPMD spectrum is corrected by a scaling constant so as to match the static structure obtained from PIMC, then it turns out to be slightly better than the corresponding FK-QCW one. Finally, since FK-LPI correctly reproduces both the static structure and the recoil term, this would seem to make the method preferable for high-q spectral calculations. Needless to say, one cannot completely exclude that experimental data still retain some small inaccuracies due to the complexity of the present data reduction procedure. For instance, multiple scattering corrections resorted to the Sköld approximation [23], and the removal of incoherent contributions was based on the Gaussian approximation [32]. However, if the results published in the pure liquid D_2 case [10] are also taken into account, then we can observe that the present data on mixtures confirm the general picture. On the one hand, the currently available quantum simulations methods are able to provide an overall correct description of the microscopic dynamics in a moderately quantum fluid such as deuterium. However, they manifest small but detectable discrepancies that still need to be assessed in a systematic way and depending on thermodynamic states and wave-vector values. At the same time, inelastic scattering techniques appear to have reached a level of accuracy that starts to play a discriminating role between the various computational approaches. It is reasonable to expect that further advances in both instrumental performance and simulation methods may lead to a reliable assessment of the dynamics of quantum disordered systems.

In order to clarify the physical meaning of the present spectroscopic results, a detailed analysis of the longitudinal current spectral maxima has been carried out both on neutron scattering and simulated data sets, extracting pseudophononic dispersion curves and showing a mutual agreement at the same level found in the comparison of the scattering laws. Nevertheless, the peculiarities of the D_2 center-of-mass dynamics in the mixtures were revealed only by the separate investigation of the lightweight mass components and the heavy mass components of such dispersion curves. But this is a procedure which, quite understandably, could not be accomplished in the case of the experimental data, since, there, Ne and D_2 contributions were lumped together, each one weighted by the appropriate neutron scattering cross section. As a matter of fact, one might envisage a practical separation of the mentioned spectral components only by complementing our neutron scattering data with inelastic x-ray scattering [47] measurements in the same q–ω range as that explored in this experiment, since x-ray scattering is much more strongly affected by Ne atoms than by D_2 molecules. However, this possible scientific proposal, although clearly feasible [48], is out of the scope of the present study, representing just a possibility for further investigation on the subject of liquid mixtures exhibiting nonnegligible quantum effects. After using the neutron scattering data to check and validate quantum

simulation results, we continued our study with the modifications of the pseudophononic dispersion curves induced by the caging effect of neon on the D_2 collective dynamics. To this aim, a comparison with the CMD results obtained for the D_2 center-of-mass self-dynamics in the same liquid mixtures was proposed. Although the two physical quantities, i.e., dispersion curve and velocity autocorrelation spectrum, probe different dynamical aspects of the disordered systems under investigation, striking analogies have been found, giving rise to a more comprehensive picture of the D_2 center-of-mass microscopic dynamics and its evolution as the deuterium concentration reduces and the mixture gets more and more dense: lightweight mass dispersion curves become rather flat and somehow similar to an opticlike mode, at least up to medium values of q (say, 22–25 nm^{-1}); whereas the velocity autocorrelation spectra for D_2 centers of mass depart from the expected liquidlike behavior (i.e., a monotonic decreasing trend) by lowering the diffusion coefficient and developing a characteristic hump, which is more typically solidlike. In other words, these D_2 center-of-mass spectra start to exhibit a clear and strong maximum at nonzero frequencies and then slowly decrease with a long tail. Finally, this revealing correspondence between dispersion curves and velocity autocorrelation spectra has been studied in the interesting, although rather speculative, case of a single D_2 impurity contained in bulk liquid Ne by extrapolating CMD simulated data. Here Ne caging effects are so intense that the impurity diffusion coefficient drops to a value that is about one half of that found in sample No. (4), and the D_2 translational mean kinetic energy becomes 19% higher. In parallel, the lightweight mass dispersion curve loses all its oscillations retaining just a smooth growing trend as q increases. In conclusion, even though the present study contains high-quality neutron spectra of low-temperature Ne-D_2 liquid mixtures in the crossover regime between generalized hydrodynamics and single-particle behavior, further experimental effort is surely desirable on this system as well as on analogous D_2 mixtures with liquid Ar. In particular, it is greatly recommended that high-resolution neutron (and x-ray) Brillouin scattering studies on the collective dynamics of these liquids are performed in the wave-vector transfer range 1 nm^{-1} < q < 10 nm^{-1}, where generalized hydrodynamics surely applies and unexpected and intriguing modifications of the dispersion curves might be discovered as in the well-known Ne-He supercritical mixture [49].

APPENDIX

As shown in the scientific literature devoted to neutron and x-ray scattering from mixtures (see, e.g., Ref. [50]),

several different formalisms exist and are currently employed to represent the partial contributions to both double and single differential cross section of the system under investigation. For this reason, in the present Appendix we want to clearly define what we mean by the simulated *partial intermediate scattering function $F_{\alpha,\beta}(q,t)$*, where α and β can represent either a Ne atom or a D_2 center of mass. Subsequently, the simulated *self-intermediate scattering function $F_{s,\alpha}(q,t)$* will be also defined. On the contrary, the experimentally measured spectral functions will not be dealt with in the present Appendix since they include neutron scattering lengths, and, in the case of D_2, its molecular form factor, too. Once $F_{\alpha,\beta}(q,t)$ and $F_{s,\alpha}(q,t)$ are explained, the corresponding *dynamic structure factors*, namely $S_{\alpha,\beta}(q,\omega)$ and $S_{s,\alpha}(q,\omega)$, will turn out to be just the Fourier transforms of the mentioned physical quantities. If N is the total number of molecules, given by the sum of the Ne and the D_2 contributions $N = N_{Ne} + N_{D_2}$, then one can define the α-β intermediate scattering function as:

$$F_{\alpha,\beta}(q,t) = \frac{1}{N} \sum_{j=1}^{N_\alpha} \sum_{k=1}^{N_\beta} \langle \exp\left[-i\vec{q}\cdot\vec{r}_j^{(\alpha)}\right] \exp\left[i\vec{q}\cdot\vec{r}_k^{(\beta)}(t)\right]\rangle,$$

$$(A1)$$

where the first summation is extended only to the coordinates of the α particles $\vec{r}^{(\alpha)}$ and the second only to the coordinates of the β particles $\vec{r}^{(\beta)}$. Similarly, for the α self-intermediate scattering function, one can write:

$$F_{s,\alpha}(q,t) = \frac{1}{N} \sum_{j=1}^{N_\alpha} \langle \exp\left[-i\vec{q}\cdot\vec{r}_j^{(\alpha)}\right] \exp\left[i\vec{q}\cdot\vec{r}_j^{(\alpha)}(t)\right]\rangle. \quad (A2)$$

Since in a disordered system it is straightforward to prove that $F_{\alpha,\beta}(q,t) = F_{\beta,\alpha}(q,t)$, the standard definition of the overall intermediate scattering function [7], $F(q,t)$, can be simply obtained by:

$$F(q,t) = \frac{1}{N} \sum_{j=1}^{N} \sum_{k=1}^{N} \langle \exp\left(-i\vec{q}\cdot\vec{r}_j\right) \exp\left[i\vec{q}\cdot\vec{r}_k(t)\right]\rangle$$

$$= F_{Ne,Ne}(q,t) + 2F_{Ne,D_2}(q,t) + F_{D_2,D_2}(q,t), \quad (A3)$$

as in Eq. (6). Analogously, for the overall self-intermediate scattering function [7] $F_s(q,t)$, one writes:

$$F_s(q,t) = \frac{1}{N} \sum_{j=1}^{N} \langle \exp\left(-i\vec{q}\cdot\vec{r}_j\right) \exp\left[i\vec{q}\cdot\vec{r}_j(t)\right]\rangle$$

$$= F_{s,Ne}(q,t) + F_{s,D_2}(q,t). \quad (A4)$$

To conclude this Appendix, we report the relationships between the present definition of $S_{\alpha,\beta}(q,\omega)$ on one side and the well-known Faber-Ziman [51] and Ashcroft-Langreth formalisms [52] [represented by $S_{\alpha,\beta}^{(FZ)}(q,\omega)$ and $S_{\alpha,\beta}^{(AL)}(q,\omega)$, respectively] on the other:

$$S_{Ne,Ne}(q,\omega) = x[Ne]^2 \left[S_{Ne,Ne}^{(FZ)}(q,\omega) - 1\right] + x[Ne],$$

$$S_{Ne,D_2}(q,\omega) = x[Ne]x[D_2]\left[S_{Ne,D_2}^{(FZ)}(q,\omega) - 1\right], \quad (A5)$$

$$S_{D_2,D_2}(q,\omega) = x[D_2]^2\left[S_{D_2,D_2}^{(FZ)}(q,\omega) - 1\right] + x[D_2],$$

and

$$S_{Ne,Ne}(q,\omega) = x[Ne]\, S_{Ne,Ne}^{(AL)}(q,\omega),$$

$$S_{Ne,D_2}(q,\omega) = x[Ne]^{1/2}x[D_2]^{1/2}\, S_{Ne,D_2}^{(AL)}(q,\omega), \quad (A6)$$

$$S_{D_2,D_2}(q,\omega) = x[D_2]\, S_{D_2,D_2}^{(AL)}(q,\omega).$$

[1] J. Van Kranendonk, *Solid Hydrogen* (Plenum Press, New York, 1983).

[2] V. N. Grigor'ev and N. S. Rudenko, Zh. Eksp. Teor. Fiz. **40**, 757 (1961) [Sov. Phys. JETP **13**(3), 530 (1961)]; N. G. Bereznyak, I. V. Bogoyavlenskii, L. V. Karnatsevich, and A. A. Sheinina, Zh. Eksp. Teor. Fiz. **59**, 1534 (1970) [Sov. Phys. JETP **32**(5), 838 (1971)].

[3] C. K. Heck and P. L. Barrick, Adv. Cryog. Eng. **11**, 349 (1966).

[4] H. L. Frisch and Z. W. Salsburg (eds.), *Simple Dense Fluids* (Academic Press, New York, 1968), p. 289.

[5] P. Clark Souers, *Hydrogen Properties for Fusion Energy* (University of California Press, Berkeley, 1986); V. G. Manzhelii and Yu. A. Freiman (eds.), *Physics of Cryocrystals* (AIP Press, New York, 1997), pp. 105–108.

[6] B. M. Powell and M. Nielsen, Phys. Rev. B **12**, 5959 (1975).

[7] S. W. Lovesey, *Theory of Neutron Scattering from Condensed Matter* (Clarendon Press, Oxford, 1984), Vol. I.

[8] D. Colognesi, U. Bafile, M. Celli, M. Neumann, and A. Orecchini, Phys. Rev. E **92**, 012311 (2015).

[9] D. Colognesi, U. Bafile, M. Celli, M. Neumann, E. Guarini, and M. Duc Le, Phys. Rev. E **99**, 012138 (2019).

[10] E. Guarini, F. Barocchi, A. De Francesco, F. Formisano, A. Laloni, U. Bafile, M. Celli, D. Colognesi, R. Magli, A. Cunsolo, and M. Neumann, Phys. Rev. B **104**, 174204 (2021).

[11] D. Colognesi *et al.*, *Collective Quantum Dynamics in* Ne-D_2 *Liquid Mixtures*, STFC ISIS Facility (STFC ISIS Neutron and Muon Source, Harwell Oxford, 2019).

[12] A. D. Taylor, M. Arai, S. M. Bennington, Z. A. Bowden, R. Osborn, K. Andersen, W. G. Stirling, T. Nakane, K. Yamada, and D. Welz, *KEK Report 90-25 (Proceedings of the 11th Meet. Int. Collab. Advanced Neutron Sources, ICANS-XI)*, Vol. II, p. 705 (March 1991).

[13] F. Mezei and M. Russina, Proc. SPIE **4785**, 24 (2002).

[14] V. A. Rabinovich, A. A. Vasserman, V. I. Nedostup, and L. S. Veksler, *Thermophysical Properties of Neon, Argon, Krypton and Xenon* (National Reference Data Service, Moscow, 1976), Vol. 10.

[15] I. A. Richardson, J. W. Leachman, and E. W. Lemmon, J. Phys. Chem. Ref. Data **43**, 013103 (2014).

[16] D. Güsewell, F. Schmeissner, and J. Schmid, Cryogenics **10**, 150 (1970).

[17] W. B. Street, *Proceedings of the International Cryogenic Engineering Conference 2* (ISTP, London, 1968), p. 260.

[18] S. R. Challa and J. K. Johnson, J. Chem. Phys. **111**, 724 (1999).

[19] H. M. Roder, G. E. Childs, R. D. McCarty, and P. E. Angerhofer, *Survey of the Properties of Hydrogen Isotopes Below Their Critical Temperatures*, National Bureau of Standards Technical Note 641 (U.S. Government Printing Office, Washington, DC, 1973).

[20] V. F. Sears, Neutr. News **3**, 26 (1992).

[21] W. D. Seiffert, B. Weckermann, and R. Misenta, Z. Naturforsch. **25**, 967 (1970).

[22] A. K. Agrawal, Phys. Rev. A **4**, 1560 (1971); V. F. Sears, Adv. Phys. **24**, 1 (1975).

[23] K. Sköld, Phys. Rev. Lett. **19**, 1023 (1967).

[24] V. F. Sears, Can. J. Phys. **44**, 1279 (1966).

[25] M. Zoppi, Phys. B: Condens. Matter **183**, 235 (1993).

[26] J. Cao and G. A. Voth, J. Chem. Phys. **100**, 5106 (1994).

[27] I. R. Craig and D. E. Manolopoulos, J. Chem. Phys. **121**, 3368 (2004).

[28] J. A. Poulsen, G. Nyman, and P. J. Rossky, J. Chem. Phys. **119**, 12179 (2003).

[29] K. K. G. Smith, J. A. Poulsen, G. Nyman, and P. J. Rossky, J. Chem. Phys. **142**, 244112 (2015).

[30] R. P. Feynman and H. Kleinert, Phys. Rev. A **34**, 5080 (1986).

[31] H. Kim, Chem. Phys. Lett. **436**, 111 (2007).

[32] A. Rahman, K. S. Singwi, and A. Sjölander, Phys. Rev. **126**, 986 (1962).

[33] E. J. Heller, J. Chem. Phys. **65**, 1289 (1976).

[34] J. A. Poulsen, J. Scheers, G. Nyman, and P. J. Rossky, Phys. Rev. B **75**, 224505 (2007).

[35] K. K. G. Smith, J. A. Poulsen, G. Nyman, A. Cunsolo, and P. J. Rossky, J. Chem. Phys. **142**, 244113 (2015).

[36] J. J. Morales and M. J. Nuevo, J. Comput. Chem. **16**, 105 (1995).

[37] M. Faubel, F. A. Gianturco, F. Ragnetti, L. Y. Rusin, F. Sondermann, U. Tappe, and J. P. Toennies, J. Chem. Phys. **101**, 8800 (1994).

[38] I. F. Silvera and V. V. Goldman, J. Chem. Phys. **69**, 4209 (1978).

[39] S. Bellissima, M. Neumann, U. Bafile, D. Colognesi, F. Barocchi, and E. Guarini, J. Chem. Phys. **150**, 074502 (2019).

[40] B. J. Berne and G. D. Harp, On the calculation of time correlation functions, in *Advances in Chemical Physics*, Vol. 17 (Wiley and Sons, New York, 1970), pp. 63–227.

[41] J.-P. Hansen and I. R. McDonald, *Theory of Simple Liquids* (Academic Press, Cambridge, MA, 2006).

[42] D. Pines, *Elementary Excitations in Solids* (Benjamin, New York, 1964); D. Pines and P. Nozières, *The Theory of Quantum Liquids* (Benjamin, New York, 1966).

[43] A. A. van Well and L. A. de Graaf, Phys. Rev. A **32**, 2396 (1985).

[44] D. J. González, L. E. González, J. M. López, and M. J. Stott, Europhys. Lett. **62**, 42 (2003).

[45] V. F. Sears, Proc. Phys. Soc. **86**, 953 (1965); Y. Nakahara and H. Takahashi, *ibid.* **89**, 747 (1966); Y. Fukui and T. Morita, J. Phys. C: Solid State Phys. **3**, 1839 (1970).

[46] J. A. Poulsen, G. Nyman, and P. J. Rossky, J. Phys. Chem. A **108**, 8743 (2004).

[47] W. Schülke, *Electron Dynamics by Inelastic X-Ray Scattering* (Oxford University Press, Oxford, 2007), pp. 99–145.

[48] A. Cunsolo, G. Pratesi, R. Verbeni, D. Colognesi, C. Masciovecchio, G. Monaco, G. Ruocco, and F. Sette, J. Chem. Phys. **114**, 2259 (2001).

[49] U. Bafile, P. Verkerk, E. Guarini, and F. Barocchi, Phys. Rev. Lett. **86**, 1019 (2001); M. G. Izzo, F. Bencivenga, A. Gessini, A. Cunsolo, and C. Masciovecchio, Philos. Mag. **91**, 1767 (2011).

[50] D. A. Keen, J. Appl. Cryst. **34**, 172 (2001).

[51] T. E. Faber and J. M. Ziman, Philos. Mag. **11**, 153 (1965).

[52] N. W. Ashcroft and D. C. Langreth, Phys. Rev. **156**, 685 (1967).